Ultrahigh-Resolution, Deep-Penetration Spectral-Domain Optical Coherence Tomography

by

Liane Bernstein

Submitted to the
Department of Electrical Engineering and Computer Science
in Partial Fulfillment of the Requirements for the Degree of

Master of Science

at the

MASSACHUSETTS INSTITUTE OF TECHNOLOGY

September 2018

Author: Signature redacted
Department of Electrical Engineering and Computer Science
August 31, 2018

Certified by: Signature redacted
Seok-Hyun (Andy) Yun, Professor of Dermatology at Harvard University
Thesis Supervisor

Certified by: Signature redacted
Roger G. Mark, Professor of HST and EECS at MIT
Thesis Co-Supervisor

Accepted by: Signature redacted
Leslie A. Kolodziejski
Professor of Electrical Engineering and Computer Science
Chair, Department Committee on Graduate Students

Ultrahigh-Resolution, Deep-Penetration Spectral-Domain Optical Coherence Tomography

by

Liane Bernstein

Submitted to the Department of Electrical Engineering and Computer Science on August 31, 2018, in Partial Fulfillment of the Requirements for the Degree of Master of Science in Electrical Engineering and Computer Science at the Massachusetts Institute of Technology

ABSTRACT

Optical coherence tomography (OCT) is a label-free optical imaging modality that allows non-invasive in-depth visualization of microscopic structures in samples. With a typical resolution of 10-15 μm and a penetration of up to a few mm, OCT is widely used for medical diagnoses in fields such as ophthalmology and cardiology. However, the more common diagnostic tool in the microscopic regime of medical imaging is histology, an invasive technique requiring tissue biopsy. Its resolution can be as small as 0.2 μm, allowing the visualization of subcellular structures. To help bridge this gap between OCT and histology, ultrahigh-resolution OCT systems have been developed, with resolutions on the order of 1 μm. Yet their application remains limited, since they employ shorter-wavelength sources, reducing penetration in tissue.

We have designed and built a spectral-domain ultrahigh-resolution, deep-penetration OCT system centered at 1290 nm with axial and lateral resolutions of 2 and 5 μm, respectively. To our knowledge, this is the best axial resolution obtained for a high-speed OCT system centered this deeply in the infrared. We demonstrate imaging of the cardiac conduction system, which could eventually be used for intraoperative identification of conducting tissue. In addition, we show images of the corneo-scleral angle, which could help properly diagnose primary angle-closure glaucoma. Other potential applications are also discussed.

Thesis Supervisor: Seok-Hyun (Andy) Yun
Title: Professor of Dermatology at Harvard University

Thesis Co-Supervisor: Roger G. Mark
Title: Distinguished Professor of HST and of EECS at MIT

Acknowledgments

I would like to extend my thanks to Prof. Andy Yun for his guidance and support, and for sharing his vast knowledge of OCT with me. Thanks also to Prof. Roger Mark for his encouragement throughout this project.

This work would not have been possible without my colleagues in the Yun Lab. Specifically, thanks to Antoine Ramier for help with data processing and valuable scientific discussions. Thanks to Jiamin Wu for crucial assistance with the spectrometer design in Zemax, Dr. Amira Eltony for helpful insights, and Brian Battersby for writing the C++ data acquisition software and real-time display interface. Thanks also to Dr. Marie Béland for her support, and for the idea to image the cardiac conduction system. Thanks to Dr. Vera Aiello for help with OCT image interpretation in the heart, and for providing histology images of porcine hearts. Last but not least, thanks to my family and friends, especially my husband Aakash Ravi, my partner in goofiness, rock climbing, science and life, for invaluable scientific discussions, support and encouragement.

I was supported by the *Fonds de recherche du Québec – Nature et technologies* (FRQNT) and by the National Institutes of Health under award P41-EB015903, Center for Biomedical OCT Research and Translation.

Table of Contents

List of Figures

List of Tables

CHAPTER 1

Introduction

1.1 Optical Coherence Tomography

Optical coherence tomography (OCT) is a label-free optical imaging modality that allows non-invasive in-depth visualization of microscopic structures in samples. The basic principle behind OCT is that echo time delays of light are measured via interferometry, to achieve a resolution of typically 10-15 μm and an imaging depth of up to a few millimeters. This technology was invented in the early 1990s [1], and in the short time since then, OCT has been used in a wide variety of fields. The most wide-spread use of OCT has been in ophthalmology, in which this technology is now the standard-of-care for retinal imaging [2]. Some other notable examples are in cardiology to image plaques in coronary arteries endoscopically [3], in oncology to image cancerous tumors [4] and in gastroenterology to image the gastrointestinal tract [5]. Outside biomedicine, OCT has also been applied in numerous fields, such as art restoration [6] and the inspection of glass, optical components and polymers [7].

An important limitation of standard OCT systems, keeping this technology from becoming truly ubiquitous in the world of microscopy, is its resolution. By contrast, the more common diagnostic tool in the microscopic regime of medical imaging is histology, where tissue is sliced very thinly, stained, and observed under a standard microscope, with a resolution as small as 0.2 μm [8]. This centuries-old technique allows clinicians to observe individual cells and surrounding structures in order to identify regions of interest such as tumor margins.

Recently, the resolution gap between OCT and histology has been narrowing, with developments in ultrahigh-resolution OCT (UHR-OCT) leading to images with cellular-scale resolution (~1 μm). For instance, Liu et al. built an OCT system with a resolution of 2 μm x 2 μm x 1 μm (x, y, z) in tissue, which they used to image

coronary plaques [9]. Others have pushed the resolution limit even further, with, to our knowledge, the best OCT axial resolution in tissue reaching 0.5 μm [10], [11]. To achieve this higher resolution with OCT, imaging must be done at shorter wavelengths and/or with a wider spectral bandwidth than typical systems. Since UHR-OCT tends to use shorter wavelengths, its application is limited due to reduced penetration in scattering biological tissues (a few hundred micrometers) [12], [13].

The objective of this project is to design and build an ultrahigh-resolution, deep-penetration OCT system that can be used to visualize structures deeper in biological tissues at the cellular level. Key to higher-resolution and deeper-penetration imaging is the use of an ultra-broadband light source that produces longer wavelength radiation in the infrared, where loss of signal from tissue scattering is diminished [12], [13]. Another advantage of using longer-wavelength light is that a higher laser power can be used, since longer-wavelength radiation is less damaging to tissue [14].

It is worthwhile to note that UHR-OCT has previously been demonstrated deeper in the infrared than the afore-mentioned Refs. [9]–[11]. For instance, UHR-OCT imaging has been performed with a 470 nm bandwidth source at a central wavelength of 1375 nm [15] and a 350 nm bandwidth source centered at 1300 nm [16]. However, only *ex vivo* tissues were imaged with an impractical and slow technique (time-domain OCT). Other groups (research and commercial) with high-speed OCT systems that have a larger penetration depth have axial resolutions of 10-15 μm (see, for example, Refs. [17]–[19]). Thus, the combination of cellular-level resolution, deep-penetration and high imaging speed has not previously been realized, to the best of our knowledge.

1.2 Basic Optical Coherence Tomography Theory

An OCT system is essentially a low-coherence interferometer, in which large-bandwidth laser light is incident on a sample, and the light backscattered by structures at different depths in the sample is collected. Figure 1 shows an OCT system in its

simplest form, producing a 1D reflectivity profile across a sample depth of up to a few millimeters, commonly called A-line.

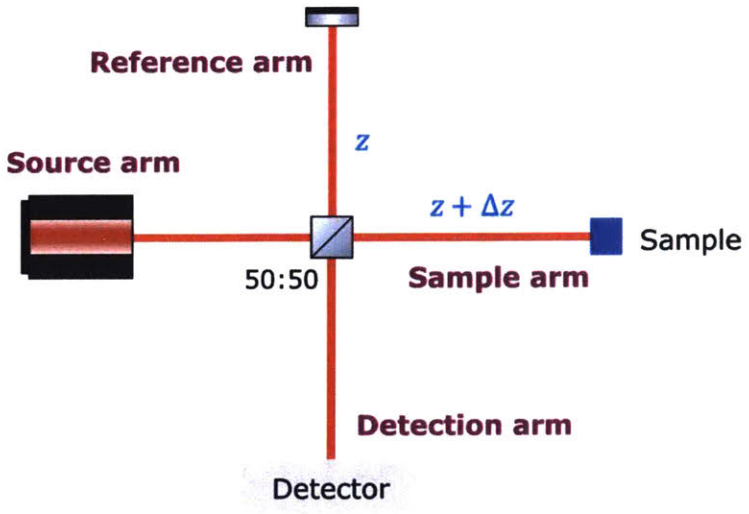

Figure 1: Basic OCT system producing a 1D sample reflectivity profile (A-line)

In the detection arm, the light backscattered from a structure in the sample arm at a distance $z + \Delta z$ from the 50:50 beamsplitter interferes over a short distance with light from the reference arm of the interferometer. The reflectivity profile of the sample can then be reconstructed using a spectrometer in the detection arm, using a technique called spectral-domain OCT (SD-OCT), which will be explained below. Following a similar development to Ref. [20], it can be shown that light from a single reflector with reflectivity r_s in the sample arm at position $z + \Delta z$ produces the following intensity in the detector arm, called interferogram:

$$I_{\text{det}} = \frac{1}{4} I_{\text{source}}(k)\left(1 + r_s + 2\sqrt{r_s}\cos(2k\Delta z)\right) \tag{1}$$

where $I_{\text{source}}(k)$ is the source spectrum, $k = 2\pi/\lambda$ is the wavenumber, and λ is wavelength.

Equation (1) can most simply be thought of in terms of intensity as a function of delay $I_{\text{det}}(\Delta z)$. From this perspective, it is possible to reconstruct the intensity as a function

of depth by axially scanning the reference arm, with a single time-resolved point detector in the detection arm. This technique is called time-domain OCT, or TD-OCT.

If instead, we look at equation (1) as intensity as a function of wavenumber $I_{\text{det}}(k)$, we recognize that all delays can be captured simultaneously by placing a spectrometer in the detection arm. Indeed, $I_{\text{det}}(k)$ is measured on the spectrometer, and the interferogram that is obtained (equation (1)) can then be processed with an inverse Fourier transform ($k \rightarrow z$) to allow the determination of the path length difference, or delay Δz:

$$I_{\text{det}}(z) = \frac{1}{4} ifft\{I_{\text{source}}(k)\} * \left((1 + r_s)\delta(z) + 2\sqrt{r_s}(\delta(z - 2\Delta z) + \delta(z + 2\Delta z))\right) \quad (2)$$

Equation (2) shows that there are peaks at $\pm 2\Delta z$ that have the shape of the inverse Fourier transform of the source spectrum. (These peaks are modulated by the sample reflectivity r_s.) The axial resolution of an OCT system, measured by the full-width at half maximum (FWHM) of the axial point spread function (PSF), is therefore given by width of the inverse Fourier transform of the source spectrum.

Assuming a Gaussian source of FWHM = $|k_2 - k_1|$, with standard deviation $\sigma = |k_2 - k_1|/(2\sqrt{2\ln(2)})$, the source's inverse Fourier transform is also a Gaussian, with standard deviation $\hat{\sigma} = 1/\sigma = 2\sqrt{2\ln(2)}\,/|k_2 - k_1|$. The FWHM of the source's inverse Fourier transform is therefore $8\ln(2)\,/|k_2 - k_1|$. Taking the factor of 2 into account in the delta function ($2\Delta z$ in equation (2)), and with $\lambda_1 = 2\pi/k_1$ and $\lambda_2 = 2\pi/k_2$, the axial resolution (FWHM) is therefore:

$$\delta z = \frac{4\ln(2)}{n} \left|\frac{2\pi}{\lambda_1} - \frac{2\pi}{\lambda_2}\right|^{-1} \quad (3)$$

where n is the refractive index of the medium, which must be considered since it alters the optical path length.

For a small FWHM $\Delta\lambda = \lambda_2 - \lambda_1$, equation (3) reduces to:

$$\delta z = \frac{2\ln(2)}{\pi n}\frac{\lambda_0^2}{\Delta\lambda} \tag{4}$$

where λ_0 is the source's central wavelength.

It is clear from equation (4) that the axial resolution depends on both the source's central wavelength and bandwidth. Furthermore, the reason for which UHR-OCT systems typically use shorter wavelength sources is clear: δz scales with λ_0^2. Conversely, a UHR-OCT system at longer wavelengths requires a significantly larger bandwidth source, increasing the complexity of the system from the more limited availability of sources, detectors, and from the challenges related to management of chromatic aberration. Hence, previous UHR-OCT studies employing large-bandwidth sources centered around 1300 nm ([15], [16]) use the time-domain method, since the complex design of a large-bandwidth spectrometer can be avoided in this way. However, TD-OCT is slow because of its mechanical moving parts, and most importantly, TD-OCT has a sensitivity that is two orders of magnitude lower than SD-OCT [21]–[23].

The development above explained the acquisition of a 1D OCT A-line. 2D OCT images (called B-scans) and 3D volumes are acquired by scanning the beam on the sample with mirror galvanometers (galvos). Further, the beam is laterally confined on the sample with an objective lens. The scanning mirrors must be relayed onto the back aperture of the objective lens to ensure telecentricity, and therefore flatness of the imaging plane. The lateral resolution depends on the numerical aperture of the objective lens (related to focal length and back aperture diameter), and the beam size on the back aperture of this objective.

The lateral spot size ($2w_0$ = $1/e^2$ spot diameter) can be calculated from Gaussian optics, assuming a perfect lens [24]:

$$2w_0 = \frac{4\lambda f}{\pi d} \tag{5}$$

where λ is the wavelength, f is the focal length of the lens and d is the beam size on the back aperture of the objective ($1/e^2$ diameter).

Another key specification of an OCT system is its maximum imaging depth. We define 3 important and distinct parameters of imaging depth: the depth of focus (DOF), the imaging range, and tissue penetration. The DOF is defined as the axial distance over which the beam size doubles in diameter from its smallest point (focal spot). See Figure 2 for a visual representation.

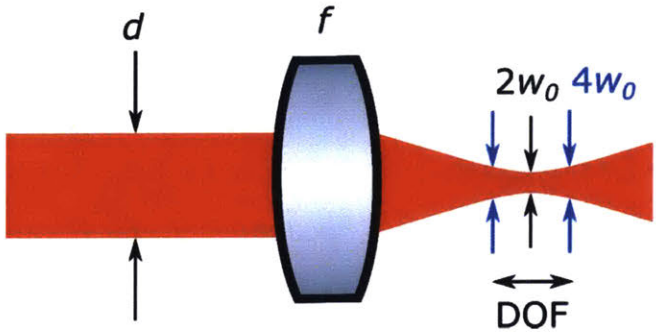

Figure 2: Axial depth of focus (DOF) achieved with a Gaussian beam of diameter d *and focal length* f

The axial DOF is given by [25]:

$$\text{DOF} = \frac{8\lambda f^2}{\pi d^2} \tag{6}$$

Therefore, the axial DOF can be related to the lateral spot size with:

$$\text{DOF} = \frac{2\pi}{\lambda} w_0^2 \tag{7}$$

From equation (7), we note that there is a compromise between lateral resolution and DOF; as lateral resolution is improved, imaging depth is reduced, since a more tightly focused beam diverges faster. If the beam has diverged too much, there will not be sufficient light returning to the spectrometer to observe a signal.

Second, the imaging range (which we call z_{max}) is related to the finite spectral sampling of the spectrometer, and represents the axial depth that can be imaged in one spectrometer acquisition. It is described by equation (8) [20]:

$$z_{max} = \frac{n{\lambda_0}^2}{4\delta\lambda} \tag{8}$$

where $\delta\lambda$ is the wavelength spacing of the spectrometer. In a standard OCT system, z_{max} is the maximum sample depth that can be imaged (not considering sample properties). Indeed, a larger axial path length difference Δz between the sample and reference arms means a higher spatial frequency of oscillation on the camera (see equation (1)). Once the frequency reaches the Nyquist limit, the interferogram can no longer be correctly sampled by the spectrometer, and thus, the depth limit has been reached. This can also lead to signal pollution with artifacts from aliasing, but usually the signal is much stronger in the non-aliased region than the aliased region of the image because of losses due to absorption and scattering of the sample.

It is, however, possible to double the depth range by implementing a scheme that allows the acquisition from $-z_{max}$ to $+z_{max}$. Because a single reflector creates two peaks after inverse Fourier transforming the signal at the detector (equation (2)), positive and negative delays $\pm\Delta z$ cannot be distinguished. This problem, called complex conjugate artifact, can be avoided by setting the zero delay point to be the start of the sample, and allowing only positive delays. In this case, the maximum depth range is z_{max}. However, if the complex signal can be reconstructed, then the ambiguity between positive and negative delays is lifted. This can be done following a procedure outlined in Refs. [20], [26]–[28], achieving "full-range OCT". In brief, by modulating the phase of the reference signal, it is possible to reconstruct the complex interferogram.

Third, tissue penetration depth is the maximum depth in a sample at which an OCT signal can still be observed, which depends on sample absorption and scattering

properties. These properties are related to source wavelength, where it is known that scattering tends to decrease in tissue with longer wavelengths in the infrared, especially with respect to visible wavelengths [12], [13].

A final factor affecting in-depth imaging is sensitivity, which is the smallest sample signal that can be observed with respect to incident power on the sample, and is usually expressed in decibels (dB). It is limited by the noise sources in the system, notably detector noise (thermal noise), laser relative intensity noise (RIN) and shot noise [29]. When using supercontinuum sources for OCT to achieve a broad spectral bandwidth, the RIN tends to be the most important source of noise [30].

1.3 Potential Applications of Deep-Penetration UHR-OCT

Applications that would most benefit from deep-penetration UHR-OCT are for samples that are highly scattering (thus more difficult to image with short wavelengths) and that have critical features at the cellular scale, either because very small structures must be resolved, or because subtle changes in morphology can better be observed with high resolution. Based on these criteria, we have identified 3 biomedical fields that would likely benefit from this technological innovation.

1.3.1 Cardiology: Toward Intraoperative Visualization of Conduction Tissue

The heart acts as a mechanical pump, contracting and relaxing roughly once per second to send blood throughout the human body. Contraction occurs when an action potential reaches cardiac muscle tissue. This action potential propagates via conduction pathways, illustrated in Figure 3 [31]. The electrical signal is first generated in the sinoatrial (SA) node and travels through the walls of the right atrium to the atrioventricular (AV) node, which is situated at the base of the wall separating the atria (atrial septum). After reaching the AV node, the electrical impulse makes its way through the bundle of His, the only conduction pathway that exists between the atria and the ventricles. The bundle of His penetrates the myocardium between the atria and the ventricles and divides into two, forming the left and the right bundle

branches on each side of the crest of the muscular portion of the ventricular septum. The action potential is rapidly propagated through the bundle branches, or conduction "highways" in the ventricular septum, and then into the Purkinje fibers and the ventricular muscle itself. The specialized conduction fibers therefore include the AV node, the bundle of His, and the right and left bundle branches [32].

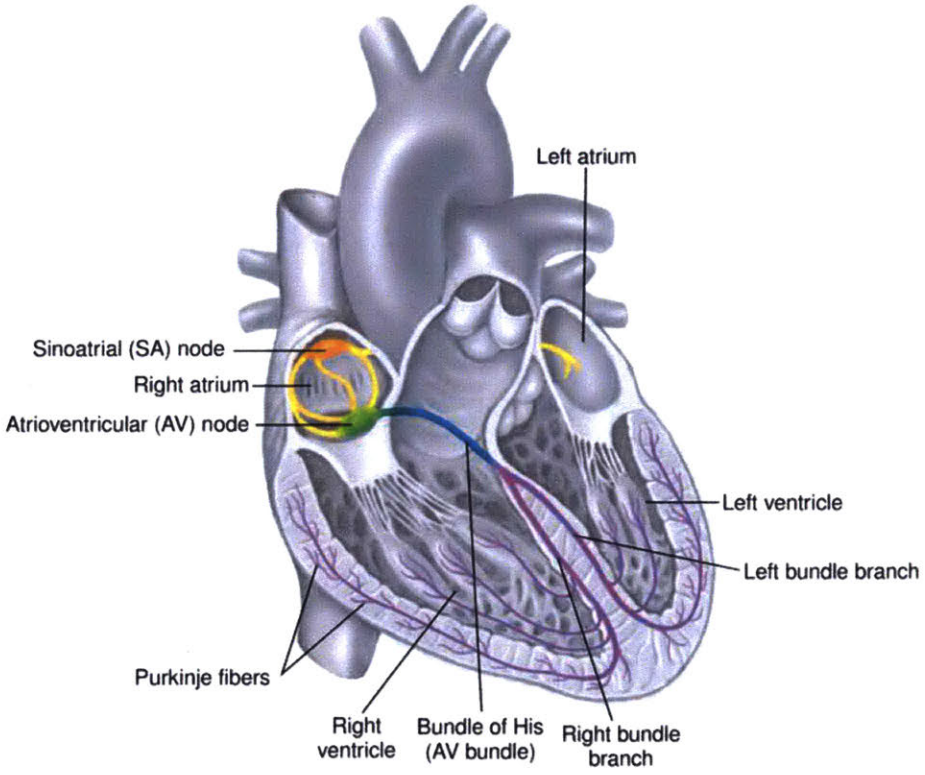

Figure 3: Conduction system of the heart [31]

These conduction pathways are not visible to the naked eye and no marker exists for conduction tissue in human hearts (except for embryonic hearts) [33]. Therefore, conduction tissue cannot be seen by a surgeon during open heart surgery. This poses a major problem when repairing congenital heart defects, since the surgeon may have to place sutures on the septum, where the important conduction pathways lie. If the surgeon places a suture on the AV node or bundle of His, he/she will cause complete heart block, by injuring or sectioning the only electrical pathway between the atria and the ventricles, thereby making a patient dependent on a pacemaker for the

remainder of his or her life. A recent retrospective study of over 100,000 open heart surgeries in pediatric patients showed that in 1% of cases, the surgery caused heart block. Furthermore, heart block was associated with higher odds of mortality [34]. An intraoperative tool that the surgeon could use to visualize and avoid injury to the conduction system would therefore be of utmost importance to reduce mortality and long-term pacemaker use in pediatric heart surgery [35].

UHR-OCT is a promising technique that could be used for this purpose. Conducting tissue generally lies within 1-2 mm of the surface of the endocardium [33], and is made up of organized fibers surrounded by collagen, which provide optical contrast. Further, the heart is stopped during open heart surgery, so there is no concern regarding motion artifacts. Lastly, the structures of interest tend to be at most tens of micrometers wide, and therefore, they are not clearly visualized on standard-resolution OCT systems.

In a recent study, the SA nodal region of an *ex vivo* canine heart was imaged with 10 μm axial and lateral resolutions [36], but low contrast and resolution led to a challenging identification of the SA node. Purkinje fibers were also seen by OCT in a different study, in an *ex vivo* porcine heart with a system centered at 840 nm and an axial resolution of 2.7 μm [37]. With deeper penetration and higher resolution, we hope to be able to image and map more of the conduction system.

1.3.2 Inner Ear

The human ear is a remarkable acoustic detector, allowing us to hear sounds with 10,000,000-fold intensity variations across a frequency band stretching from 20 Hz to 20 kHz, and with a frequency resolution of just ~3.6 Hz in the 1-2 kHz band. It is divided into three main sections: the outer, middle, and inner ear (see Figure 4). In the outer ear, sound pressure waves are conducted through the ear canal, making the ear drum vibrate. Then, three small bones in the middle ear transmit these vibrations to the inner ear. Lastly, the inner ear acts as the transducer that converts mechanical

vibrations from the middle ear into electrochemical signals to be interpreted by the brain [38].

The inner ear is composed of many fine structures, notably the Organ of Corti, which contains inner and outer hair cells (~10 μm wide). There is great interest in understanding how these structures transmit, amplify, and detect sound signals. The inner ear has been studied by *post mortem* histology, CT scan, micro-CT [39] and MRI [40]. However, the *in vivo* imaging modalities previously used to image the inner ear have resolutions on the order of 1 mm, too large to see the Organ of Corti, let alone hair cells. But imaging hair cell motion is critical, not only to understand how these cells can amplify minute vibrations, but also because they are thought to play a role in auditory degeneration.

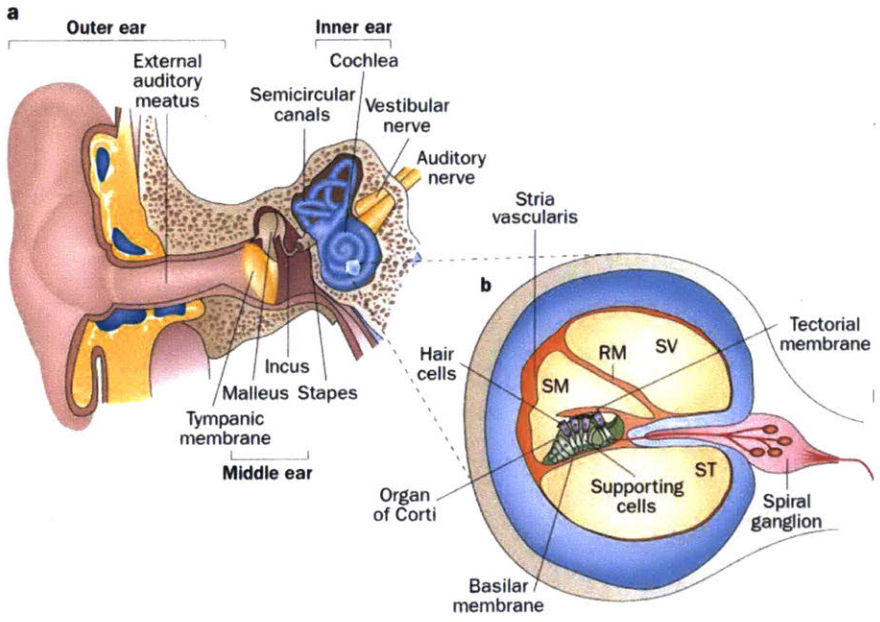

Figure 4: Basic diagram of the ear (a) and inner ear (b). Adapted from Ref. [41].

Optical coherence tomography (OCT) is a promising *in vivo* imaging modality for this application, as it has improved resolution over CT and MRI, and can achieve a penetration depth of up to a few millimeters noninvasively. Recently, Iyer et al. [42] demonstrated ultrahigh-resolution OCT imaging of fixed guinea pig ears with a

resolution in biological tissue of 2 μm x 2 μm x 1 μm. This group was able to observe hair cells *ex vivo* with their broad-bandwidth source centered at 800 nm, but the system's imaging depth was insufficient for *in vivo* studies.

We hope to use our system to study the mammalian inner ear, where we will visualize sound transmission *in vivo* and noninvasively, at the cellular level. This will require light penetration through a thin layer of cochlear bone and tissue, which we believe our deep-penetration UHR-OCT system will be able to achieve.

1.3.3 Ophthalmology

As previously mentioned, OCT is widely used in ophthalmology, especially in the posterior segment of the eye to image the retina. More recently, OCT has been used to image the anterior segment as well [22]. (For reference, a diagram of the eye is shown in Figure 5 [43].)

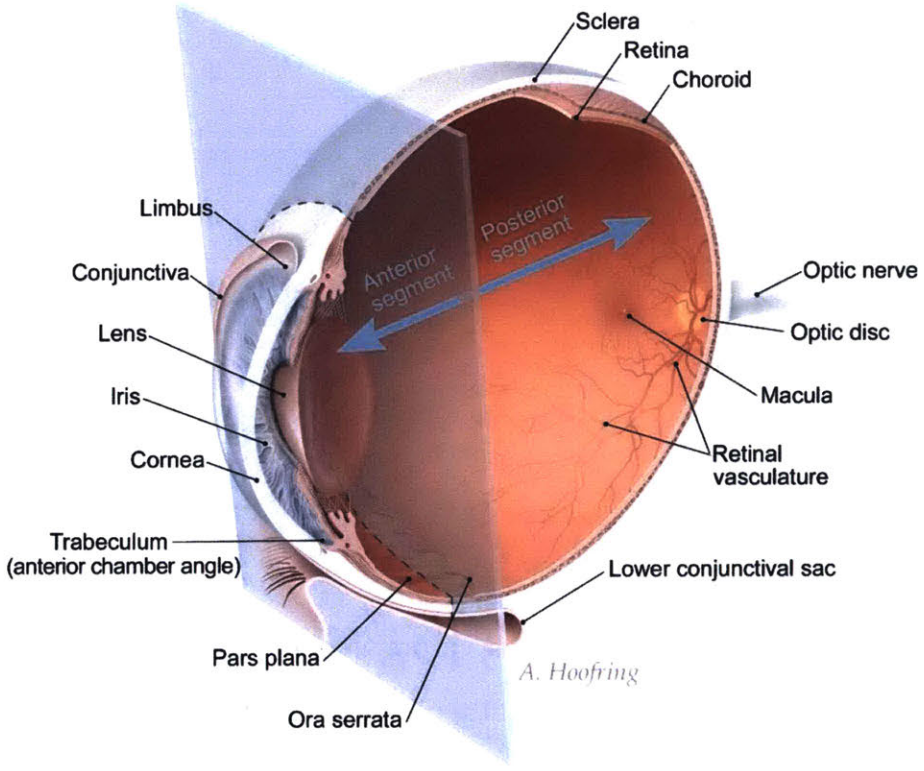

Figure 5: Schematic of the eye [43]

For instance, the cornea has been imaged with UHR-OCT, and corneal nerve bundles of a width of just a few micrometers have been resolved with a system centered at 800 nm [44]. Though this study was performed with a relatively short-wavelength system, the full width of the cornea could be visualized (since the cornea is transparent). Therefore, there is no requirement to use longer wavelengths to image the cornea.

Where the longer wavelengths are necessary is imaging in or through the sclera, which is highly scattering. OCT centered around 1300 nm has notably been used to image the region where the cornea and iris meet [45], [46]. This region is of interest because the angle formed by the cornea and sclera and the surrounding structural integrity (or lack thereof) is indicative of primary angle-closure glaucoma (PACG). In this disease, drainage of the eye through the trabecular meshwork is blocked by the iris, and can lead to blindness [47]. The prevalence of PACG is 0.4% in Europeans aged 40 or older [48], and 0.75% in Asians aged 40 or older [49]. Evaluation by gonioscopy, the standard diagnostic tool for this disease, may not show the full scale of trabecular meshwork damage [50], [51]. Thus, if the trabecular meshwork could be directly visualized, it would be an invaluable diagnostic tool. At the very least, higher-resolution imaging of the corneo-scleral angle can be helpful in correctly diagnosing PACG. Indeed, small gaps and other micrometer-scale abnormalities may be missed with lower-resolution OCT systems, prompting the investigation of using higher resolution OCT to image the corneo-scleral angle [52].

Chapter 2

Materials and Methods

This section outlines the considerations and rationale behind our deep-penetration UHR-OCT system design. It also describes the theoretical and simulated parameters of our system. Lastly, we present our methods for OCT data acquisition and processing.

2.1 System Design

2.1.1 Source Arm

As previously discussed, in OCT, the axial resolution scales with the square of the source's central wavelength, and with the inverse of the source's bandwidth. Therefore, in ultrahigh-resolution OCT, shorter wavelengths are typically used (for example, in [9], the total spectral bandwidth extends from 600-1000 nm). But to image deeper into tissue, longer wavelengths are needed. In our system, we use the spectral range from 990 to 1590 nm of a supercontinuum laser (SuperK EXTREME EXW-4 from NKT Photonics) to extend penetration depth while maintaining ultrahigh resolution. This source emits in the visible wavelength range as well, but that light is rejected with a longpass filter (Semrock BLP01-980R-25). The filter is on a flip mount, since the visible portion of the spectrum is convenient to view the laser spot on the sample. A neutral density filter is also added to reduce the power on the sample to 25 mW.

The source spectrum, with the laser set to 48% power, is shown in Figure 6. (Changing the laser power alters the spectral shape, and 48% was empirically found to have the flattest response over our wavelength band of interest.) In more detail, Figure 6 is the reference arm spectrum measured on our custom spectrometer, where the laser light travels from the source through filters, a beamsplitter, some lenses, and a photonic crystal fiber to our spectrometer. These components alter the spectrum slightly, but

do not have a large effect on the spectral shape, as they were all chosen to have a mostly uniform spectral response.

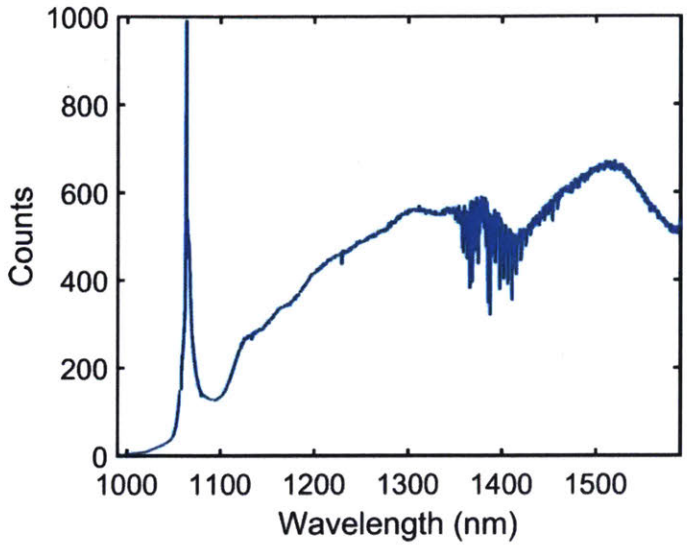

Figure 6: Spectrum emitted by supercontinuum laser (NKT SuperK Extreme EXW-4) measured on our spectrometer

2.1.2 Sample Arm (Scan Relay and Objective Lens Design)

In the sample arm, scan and tube lenses must relay the scanning mirrors onto the back aperture of the objective lens, where light is focused onto the sample. The scan and tube lenses also serve to expand the source beam.

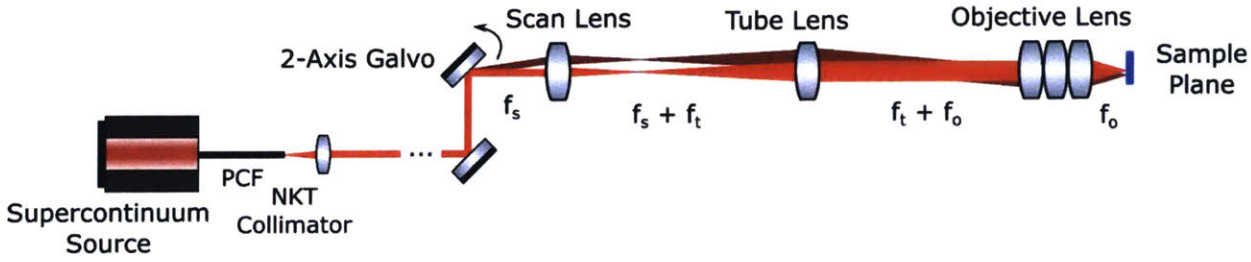

Figure 7: Sample arm design with distances shown in terms of focal lengths of scan, tube and objective lenses

A significant design challenge remains in the form of managing chromatic aberration. Lens placement, radii of curvature and materials must be chosen with care to avoid beam distortions across the entire bandwidth. Figure 7 illustrates the desired sample

arm configuration, where the focal lengths and radii of curvature of the lenses must be determined. This design assumes both galvo mirrors are close together.

Another important design consideration when using Gaussian beams is the trade-off between lateral resolution and axial depth of focus (DOF), as described in chapter 1, and illustrated in Table 1. We decided to use our system in two configurations: configuration 1 having a lateral resolution of 5 μm and a DOF of 88 μm for samples where we wanted to see more lateral details in a smaller axial field of view, and configuration 2 having a lateral resolution of 15 μm and a DOF of 790 μm for samples with finer axial details than lateral, and where information over a large axial field of view was of interest.

Table 1: Axial depth of focus corresponding to a given lateral resolution for a Gaussian beam

Lateral resolution (FWHM, μm)	Axial depth of focus (μm)
2	14
5	88
15	790
30	3160

The sample arm was modeled and optimized with the optical simulation software Zemax for three different wavelengths (990, 1300 and 1590 nm). The design goal was to obtain a FWHM lateral spot size on the sample of 5 μm for all 3 wavelengths. This design could then be adapted to obtain a FWHM lateral spot size of 15 μm, since aberrations are easier to manage when focusing less tightly.

We can first calculate the approximate focal length of objective lens that is required from an ideal Gaussian beam and objective lens. The lateral beam diameter was measured to be $d = 2.3$ mm at the galvo mirrors (Thorlabs GVS012) at a central wavelength of 1300 nm. Supposing a 1:3 telescope with perfect scan and tube lenses relaying this light onto the back aperture of the objective lens, the beam diameter on the back aperture of the objective lens is $d = 6.9$ mm. We then solve for f from

equation (5) in chapter 1, with $2w_0 = 8.5$ μm (for FWHM = 5.0 μm) to obtain $f = 35$ mm.

Zemax Modeling: Source

Initially, the source was modeled in Zemax as a collimated Gaussian beam with $1/e^2$ width and aperture width equal to the real $1/e^2$ lateral width of the laser light at the scanning mirrors. Once an initial design was established, for design refinement with accurate source modeling, laser divergence was included in the simulations.

The real divergence of the laser was first measured for different wavelengths with bandpass filters (Thorlabs, 12 nm bandwidth). For each wavelength band, a photodetector was placed at several locations along the optical axis. The laser light was partially obstructed by a razor blade mounted on a translation stage. By translating the razor blade and recording the intensity measurement for various razor locations, the beam shape (in one dimension) could be reconstructed after taking the derivative of the intensity measurements. The beam width could then be computed by fitting the resulting function with a Gaussian. It was found that visible wavelengths converge, longer wavelengths diverge, and the divergence is not significantly affected by the set laser power. The laser beam size for different wavelengths and axial locations, as well as laser angular divergence, is reported in Table 2. The divergence is defined (in radians, for small angles) as:

$$\theta = \frac{2w_2 - 2w_1}{z_2 - z_1} \tag{9}$$

where w_i is the $1/e^2$ beam width at axial distance z_i from the laser output.

This divergence was simulated in Zemax with a paraxial diverging lens (different for each wavelength in the multi-configuration editor). The beam size for each wavelength was modified by changing the focal length of a paraxial lens pair placed near the source.

Table 2: Measured beam diameter and divergence of our supercontinuum laser

Wavelength (nm)	Beam diameter* (in mm) at z = 440 mm	Beam diameter* (in mm) at z = 695 mm	Beam diameter* (in mm) at z = 1980 mm	Divergence (°)
1064 nm	1.5	1.8	3.2	0.063
1300 nm	1.9	2.3	4.1	0.079
1600 nm	2.8	3.4	6.5	0.14

*Defined here as $1/e^2$ diameter, i.e. $d = 2w$

Zemax Modeling and Optimization: Lenses

The lenses were optimized one at a time, starting from the scan lens. For each lens, the optimization procedure began with a Thorlabs achromat with a slightly longer (~50%) focal length than desired placed in the approximate focal position. Then, an additional N-BK7 lens was added, with variable radii of curvature. The distances, radii of curvature and thicknesses were then simultaneously optimized (damped least squares), first using the simple source model of a perfectly collimated source beam of $1/e^2$ diameter 2.3 mm for all wavelengths. (The Zemax optimizer was better at searching through a larger parameter space for a simpler source.) Then, the optimization was run again with the more complex multi-configuration source which considers the laser divergence. The optimization was performed over all configurations with generic merit functions and an added physical optics operand. The closest available commercial lens was selected to replace the lenses in the design, and the optimization was performed again, leaving only distances as variables. Lastly, focal length shift was characterized.

The scan and tube lenses were not found to have a significant influence on the spot size at the sample, overall aberrations or sensitivity to alignment. With long focal lengths, cemented achromatic doublets (Thorlabs) with long focal lengths placed at the foci (as indicated in Figure 7) performed similarly to optimized lens pairs. (Cemented doublets yielded spot sizes still well below the diffraction limit.) The critical component is the objective lens.

Few commercially-available microscope objective lenses exist for use with wavelengths up to 1590 nm. Further, the manufacturers of NIR objectives do not typically release data on aberrations, focal shift, dispersion, or transmission for wavelengths longer than 1300 nm. We therefore purchased an Olympus NIR objective (LMPLN5XIR) with $f = 36$ mm, and also designed our own objective in Zemax using standard Thorlabs lenses. Building an objective out of standard lenses had the added benefit of allowing us to perfectly match dispersion in the reference arm (by making a second, identical objective), and to fully understand the sources of aberrations in the system. We compare the performance of our objective versus the Olympus objective in the next chapter.

Zemax Modeling and Optimization: Objective Lens

With a regular cemented achromat used as an objective lens, we found through Zemax modeling that the desired lateral resolution cannot be achieved due to aberrations. Consequently, one may be tempted to employ an off-axis parabolic mirror (OAP) to remove considerations of chromatic aberration and dispersion. However, simple geometrical calculations and Zemax simulations show that astigmatism and coma are not manageable when an OAP is illuminated at an angle. Thus, OAPs cannot be easily implemented in scanning systems.

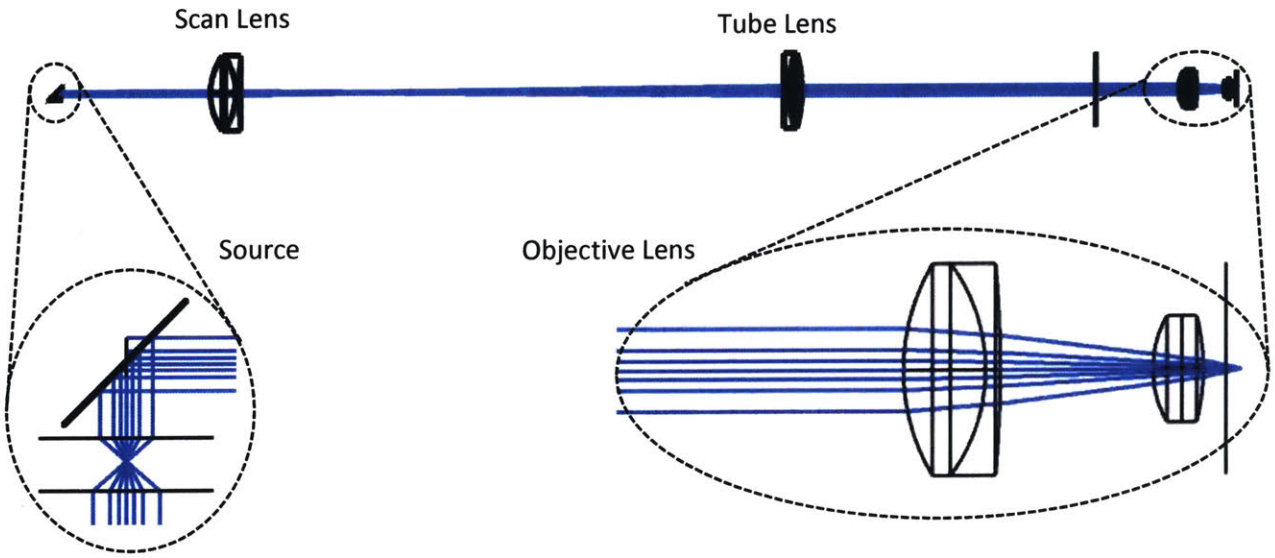

Figure 8: Final Zemax design of sample arm, after optimization and substitution with commercially-available lenses

With an $f = 100$ mm scan lens and an $f = 300$ mm tube lens, our objective lens design, optimized using the procedure described above, allows near diffraction-limited operation over the whole wavelength band with ±2° tilt of the galvo mirrors, yielding a 1.1 mm lateral field of view with limited aberrations. The final Zemax design is illustrated in Figure 8, and includes an $f = 40$ mm cemented achromat and two plano-convex lenses with $f = 25$ mm and $f = 50$ mm. The simulated FWHM spot sizes (as determined by the Physical Optics module of Zemax) are shown in Table 3, which also compares the performance of our optimized objective with the performance of single achromats. This table shows that with our optimized design, we are close to meeting our desired specification of a 5 μm spot size across the whole wavelength band, and we certainly achieve better performance than standard achromats. This is also evidenced by the reduced focal shift of our lens with respect to single achromats, as illustrated in Figure 9. Note that the shortest available focal length for an achromat with a 1-inch diameter (minimum for this design) is ~30 mm.

Table 3: Zemax-simulated spot sizes at sample for $f = 100$ mm scan lens and $f = 300$ mm tube lens (configuration 1)

Wavelength (nm)	Galvo Tilt (°)	FWHM spot size, objective is single $f = 40$ mm achromat (μm)	FWHM spot size, objective is single $f = 30$ mm achromat (μm)	FWHM spot size, optimized objective (μm)
990 nm	0	13	9.2	5.6
	2	16	11	6.6
1300 nm	0	8	6	4.1
	2	9.6	6.6	4.6
1590 nm	0	~28	~28	~10
	2	~13	~16	~14

To achieve a lateral resolution of 15 μm, the objective lens can simply be underfilled by replacing the tube lens with a cemented achromat with $f = 100$ mm. Then, the beam width d on the back aperture of the objective is decreased by a factor of 3, decreasing the lateral resolution by a factor of 3, and increasing the axial DOF by a factor of 9.

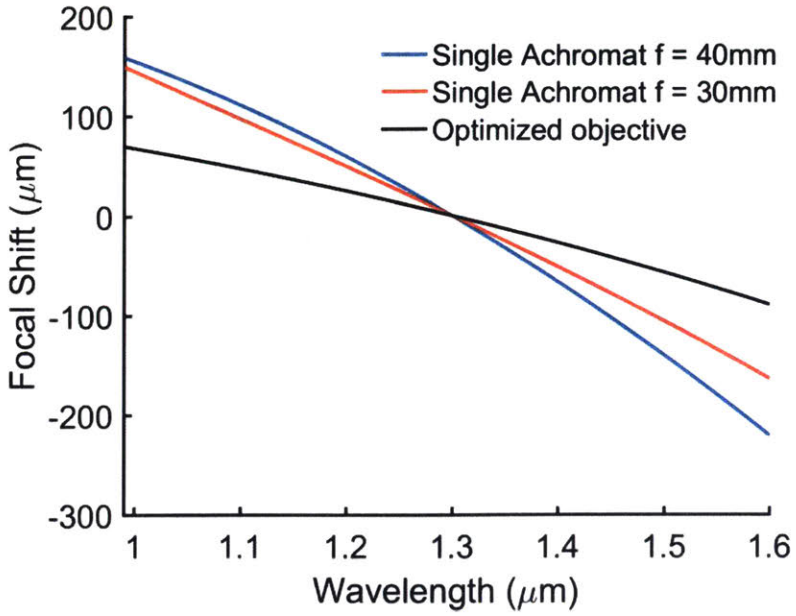

Figure 9: Comparison of focal shift of optimized objective lens versus single achromats (simulated in Zemax)

2.1.3 Reference Arm

The lenses in the reference arm are present to compensate sample arm dispersion. Indeed, a wavelength-dependent path length difference between the sample and reference arms can generate artifacts in the processed signal, as will be shown in section 2.4. The simplest way to compensate dispersion is to exactly match the sample arm lenses in the reference arm.

If a commercial objective lens is used, it cannot be perfectly matched in the reference arm unless the same commercial objective lens is purchased for the reference arm, since the types of glass and glass thicknesses are rarely disclosed. Thus, the home-built objective was used to approximately match the objective lens and the remaining dispersion was compensated numerically (section 2.4).

The reference arm mirror and reference arm objective are placed on a 1D translation stage to enable path length matching with the sample arm without altering the focusing.

Lastly, a variable reflective neutral density (ND) filter is added to the reference arm (and sample arm to compensate dispersion). The reference arm power is then optimized experimentally to maximize sensitivity, which occurs when the RIN and camera noise are balanced.

2.1.4 Detection Arm

The detection arm has the general structure illustrated in Figure 10.

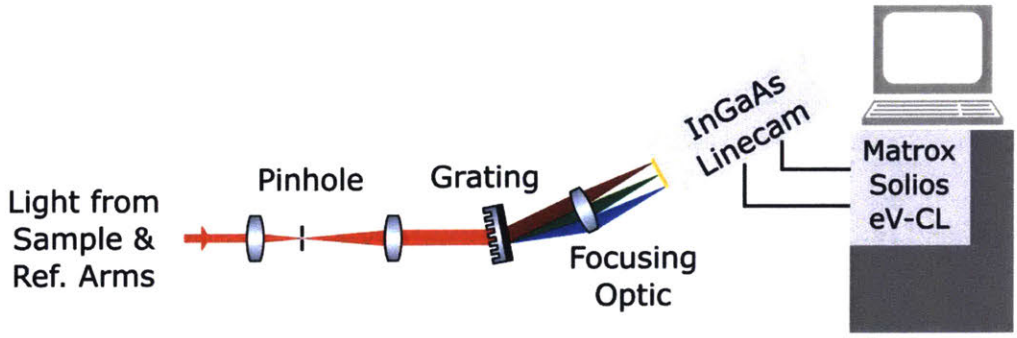

Figure 10: Generic structure of the detection arm in SD-OCT

In a typical OCT system, in the detection arm, light from the sample and reference arms is first focused through a small opening, such as a pinhole, in a 4f configuration. This ensures that light from the reference and sample arms overlaps perfectly to cause interference. Furthermore, the OCT signal-to-noise ratio is improved by the rejection of axially out-of-focus light. In our final design, we focus light into a single-mode fiber for this purpose. The small core, with a mode field diameter of 7.5 μm, acts like a pinhole, but using an optical fiber has the advantage of making the system more modular, allowing the alignment of the interferometer independently from the spectrometer. Because the fiber must be single-mode and must transmit the full wavelength band efficiently, a regular step-index fiber cannot be used. Instead, we chose an endlessly single-mode photonic crystal fiber (PCF) patchcord from Newport, which can transmit 400 to 2000 nm with low loss and with a near-constant mode-field diameter.

Spectrometer design

The most important part of the detection arm is the spectrometer. At the output of the fiber, light is collimated by a lens. Then, a transmission grating angularly splits the incident collimated light according to wavelength, as indicated by the grating equation:

$$\sin\theta_t - \sin\theta_i = l \times m \times \lambda \tag{10}$$

with θ_t the transmitted angle, θ_i the incident angle on the grating, l the number of lines per meter of the grating, m the order, and λ the wavelength. After the grating, focusing optics focus the collimated light onto the InGaAs linescan camera (GL2048R, Sensors Unlimited). A fast camera (max speed: 147,000 lines per second, or 147 klps) was chosen since we plan to, in the future, use this system to perform OCT vibrography with a procedure outlined in [53].

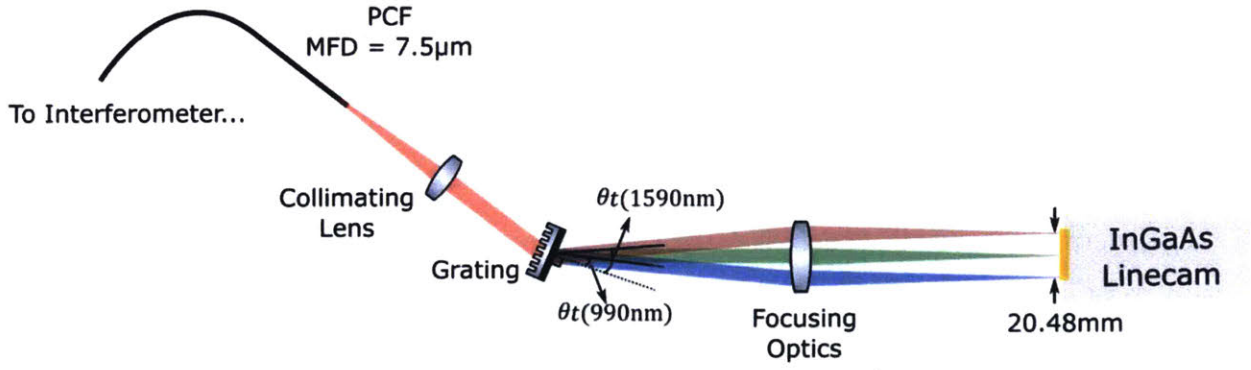

Figure 11: Structure of our detection arm

Proper spectrometer design is critical in achieving good sensitivity over a large depth (low roll-off and low signal loss). Great care must be given when using a large wavelength band to manage chromatic, as well as geometric, aberrations. Indeed, to produce low roll-off (described in section 3.2), the spot size on the camera from a monochromatic source should be smaller than the camera pixel size.

The initial constraints on the design are the line scan camera specifications, the fiber mode field diameter (MFD = 7.5 μm) and the wavelength band. The camera has 2048

pixels of size 10 μm (pitch) × 210 μm (height). Therefore, the reddest (1590 nm) and bluest (990 nm) wavelengths must be separated by 20.48 mm. Furthermore, the spot size must be smaller than 10 μm in length (y axis) by 210 μm in height (x axis). The components that must be chosen are the: **collimating lens**, **grating**, and **focusing optics**. A schematic depicting this design is shown in Figure 11.

It is easiest to align and minimize aberrations with longer focal lengths (f). To do so, a **grating** with small l (lines per meter) should be used. The lowest l for our wavelength band readily available from Wasatch Photonics was 600 lines/mm, so that is the grating we selected for our spectrometer. (We also checked that different orders would not overlap over the whole wavelength band.) The transmission angles θ_t were then fixed, with $\theta_t(990\text{nm}) = 7.4°$ and $\theta_t(1590\text{nm}) = 29.3°$.

Next came the design of the focusing optics. The desired focal length was calculated using simple geometry from the angles and distances described above, and was found to be 50 mm, where the optics must be at least 2 inches in diameter to accommodate all angles from the grating. (This, in turn, means that the **collimating lens** after the fiber must have a focal length of at least 50 mm for the $1/e^2$ diameter of the spot on the camera to be smaller than 10 μm – the camera pixel length. A simple 1-inch cemented achromat with f = 50 mm (Thorlabs) was chosen as a collimating lens.)

The **focusing** optics were designed by ray-tracing and optimization on Zemax. The input light was simulated as a perfectly collimated beam with an aperture size of 11.2 mm containing wavelengths of 990, 1300, and 1590 nm. A perfect grating was inserted, then a cemented achromat (Thorlabs) with a slightly longer focal length than the desired focal length (used achromat with f = 80 mm, desired f = 50 mm). N-BK7 lenses were added before and after the cemented achromat with variable distances and radii of curvature. A generic merit function was then applied from the Zemax optimization wizard, minimizing the RMS spot size along the camera line dimension (y). The design was not diffraction-limited after optimization, therefore another

degree of freedom was added: lateral translation of the source and grating. The final design is shown in Figure 12, with a plano-convex lens with $f = 150$ mm, a cemented achromat with $f = 80$ mm, and a positive meniscus lens with $f = 150$ mm (Thorlabs).

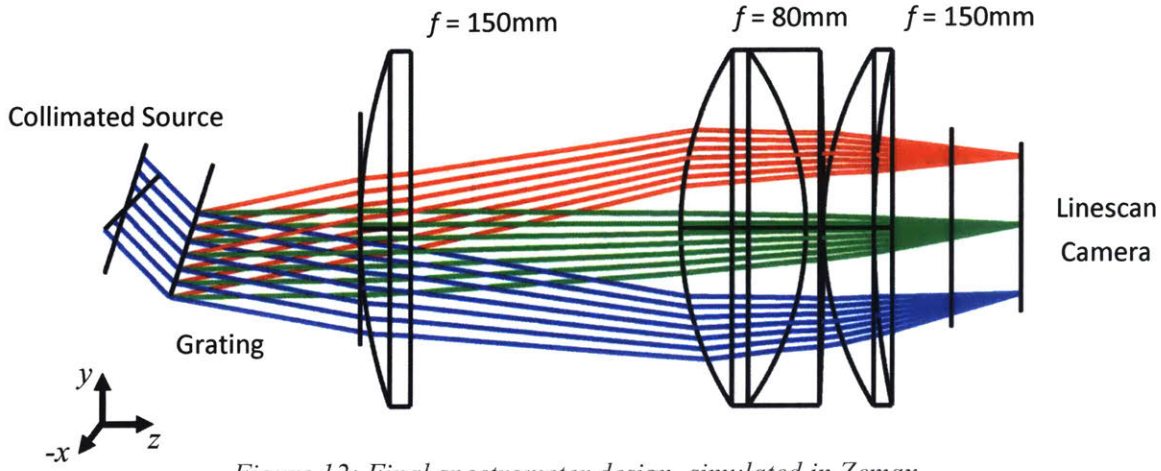

Figure 12: Final spectrometer design, simulated in Zemax

The diffraction-limited RMS spot size in y (along the camera axis) of our design, across the whole wavelength band, is shown in the top panel of Figure 13. We also compared our optimized design with a simpler one, where a pair of two $f = 100$ mm cemented achromats (Thorlabs) were used to focus light onto the camera. In this latter case, aberrations dominate and cause the spot size along the camera axis to be much larger than 10 μm. This is true even when distances between the optical components are optimized in Zemax to minimize the spot size in y. Indeed, the simulated RMS spot size in y only reaches the diffraction limit for a narrow wavelength band and is several times larger for other wavelengths, as is apparent in the top panel of Figure 13.

The bottom panel of Figure 13 shows the RMS spot size in x (perpendicular to the camera axis) for both the optimal focusing optics and the simple 2 achromat design. In both cases, though the spot is clearly aberrated, it remains well below the camera pixel height.

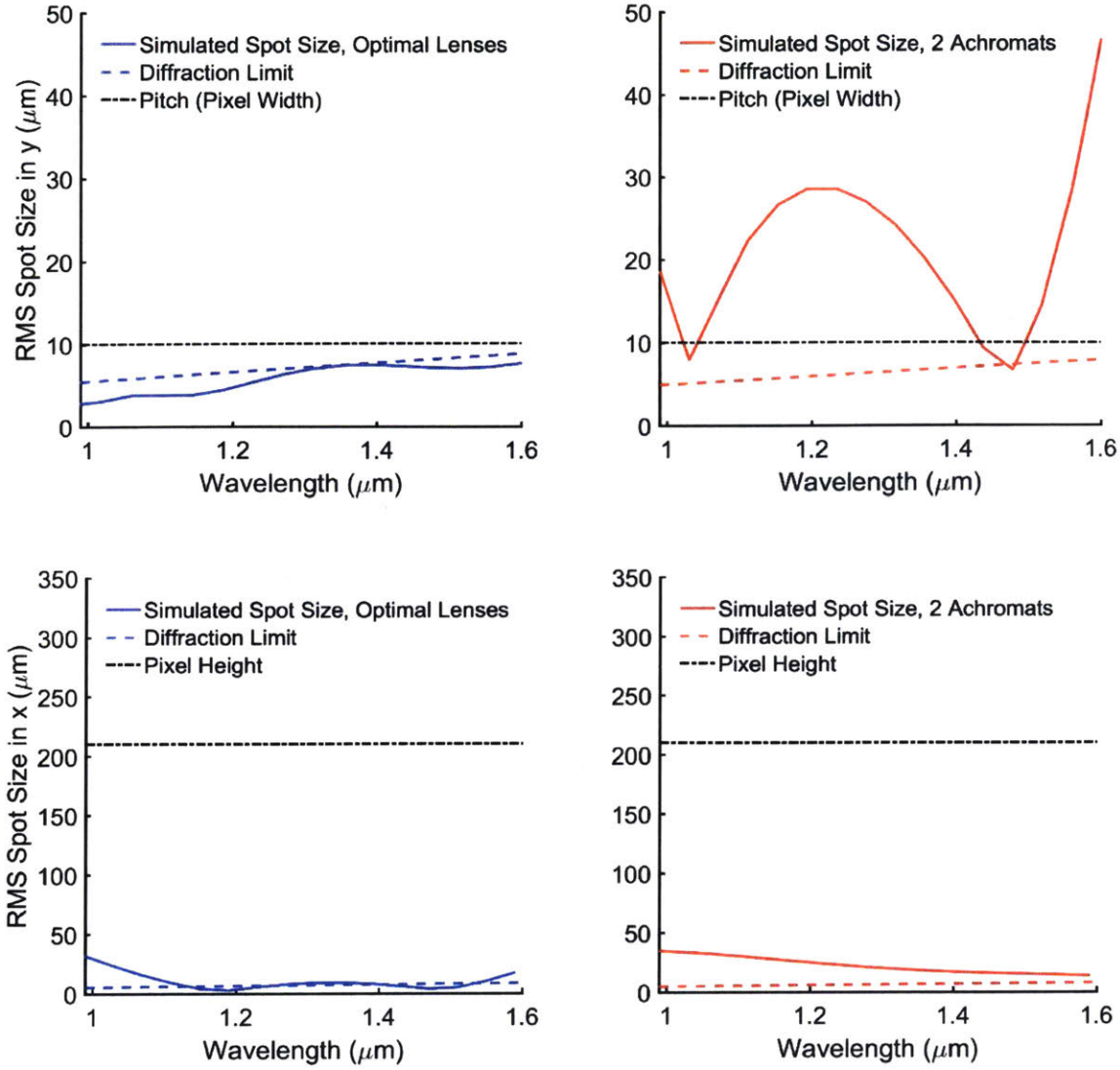

Figure 13: Comparison of RMS spot size at camera along camera axis (top) and perpendicular to camera axis (bottom) using an optimized lens triplet versus two cemented achromats for focusing. Dotted black line shows upper limit of desired spot size.

All of this being said, in our final optimized spectrometer design, the focused spot remains aberrated. Table 4 shows the simulated spots (in the x, y lateral plane, i.e. perpendicular to the axial dimension) for wavelengths of 990, 1300 and 1590 nm. The Physical Optics module of Zemax was used to generate these plots, with the incident $1/e^2$ beam diameter appropriately varied according to wavelength. Though aberrations are present, the spots are reasonably well confined along y, and are smaller than 210 μm along x. Therefore, this design was deemed acceptable for our spectrometer.

Table 4: Zemax-simulated spots (in x,y) at camera for optimized focusing optics versus 2 achromats

λ (nm)	Optimized Objective (x,y axes in mm)	2 Achromats (x, y axes in mm)
990	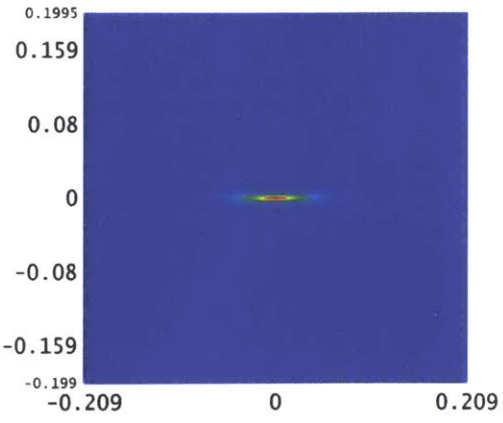	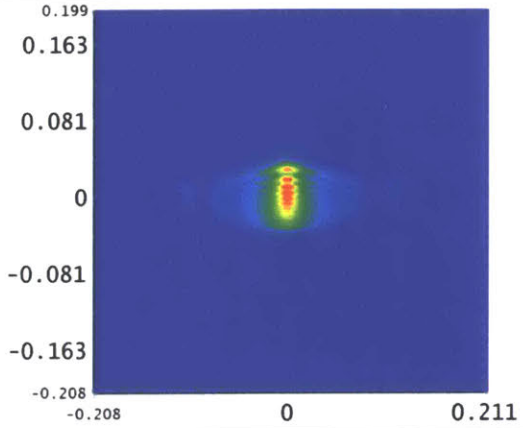
1300	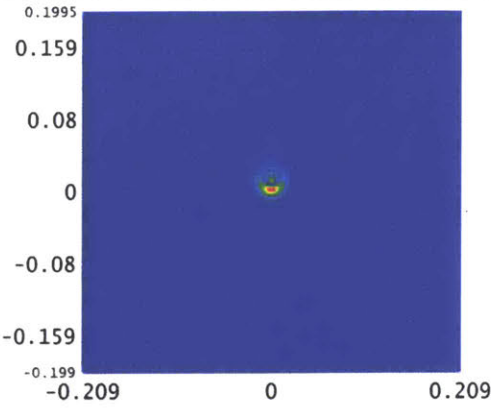	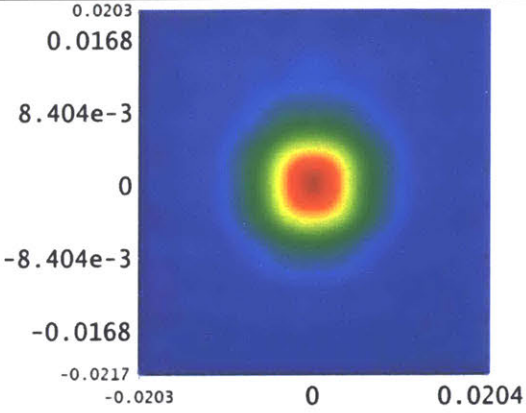
1590	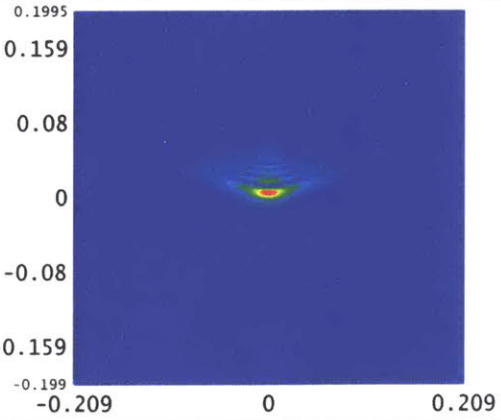	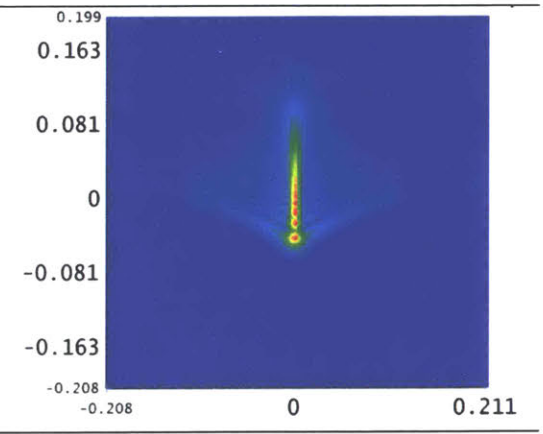

2.1.5 Complete System

Our complete system is shown in Figure 14.

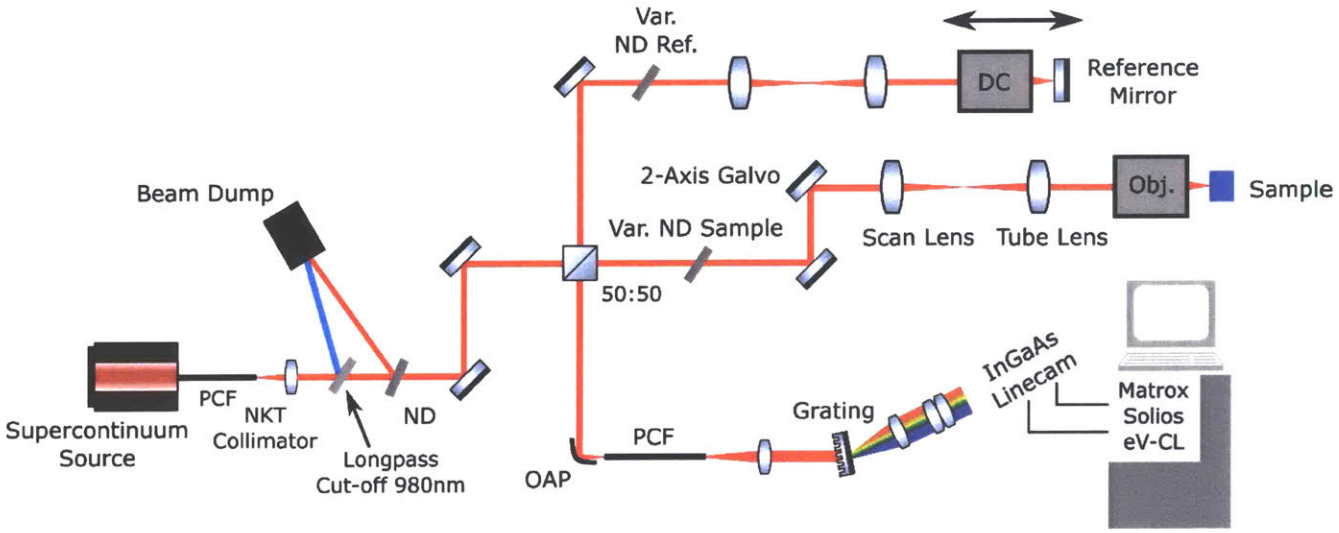

Figure 14: Schematic of our complete system

2.2 Theoretical Specifications of our System

Table 5 summarizes the specifications of our system as predicted by Zemax simulations (lateral resolution), and as calculated from equations (3), (7) and (8).

Table 5: Theoretical system specifications (in 2 different configurations)

Axial resolution* in air (μm)	1.8
Lateral resolution* in air (μm)	5/15
Center Wavelength (nm)	1290
A-line rate (klps)	10-146
Imaging range in air (mm)	1.4
Depth of focus in air (μm)	88/790

*Resolution measured as FWHM at focus

2.3 Data Acquisition

The camera in the spectrometer is connected by two Camera Link cables to a PCIe Camera Link board (Matrox Solios eV-CL). The links serve both to trigger the camera and to transmit data from the camera to the PC. (Triggers are generated in the PC and simultaneously sent to the galvo mirrors and the camera.) The raw pixel values from the camera, or interferogram, are then quickly processed to display images in real time using in-house software coded in C++. The full processing is performed later in MATLAB from the raw data.

2.4 Data Processing

Recorded on the camera from the complete system shown in Figure 14 is a raw interferogram, where the camera pixel number is linear in wavelength. An example interferogram, acquired at 146 klps, is presented in Figure 15, with a mirror in the place of the sample, and approximately equal power in the sample and reference arms (optical density of ND filter in reference arm $\approx$ optical density of ND filter in sample arm).

This interferogram must then be processed to yield interpretable data. The processing includes:

- Background subtraction;
- Envelope normalization (dividing by the source spectrum);
- k-mapping (on the camera, the signal is linear in wavelength λ, but it must be resampled to be linear in $k = 2\pi/\lambda$);
- Numerical dispersion compensation;
- Fourier transform ($k \rightarrow z$);
- z-scaling to assign delay values in μm.

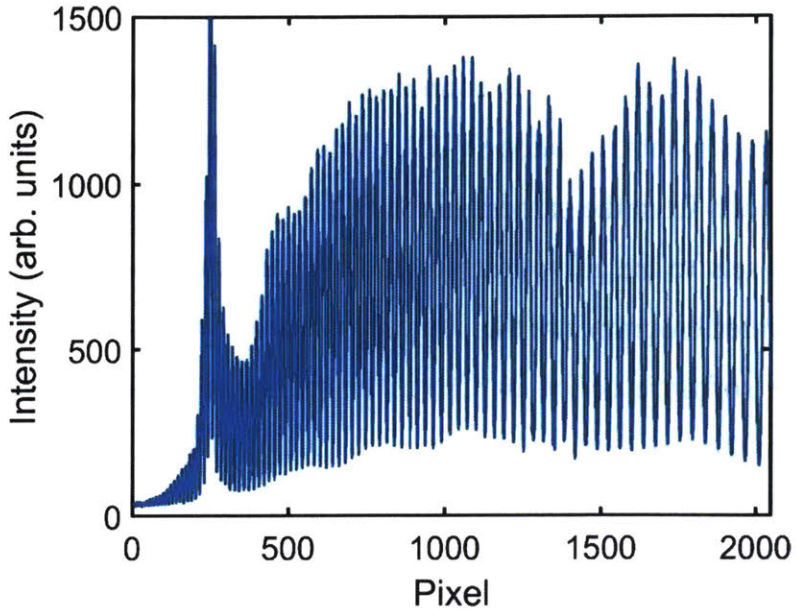

Figure 15: Example interferogram with equal optical power in sample and reference arms

It is important to note that equation (1) in chapter 1 describing the intensity observed at the detector $I_{\mathbf{det}}(k)$ assumes that the sample and reference arms are perfectly optically matched. However, differences in optical components in the sample and reference arms can add another term to this equation. In fact, different wavelengths, or wavenumbers, of light travel at different speeds through optical components such as glass (the refractive index of glass is dependent on wavelength), a phenomenon called dispersion. Therefore, if there is a mismatch in the thickness or type of glass between the sample and reference arms, the signal will be distorted by a wavenumber-dependent phase $\varphi(k)$ [54], [55]. Equation (1) then becomes equation (11):

$$I_{\mathbf{det}}(k) = \frac{1}{4} I_{\mathbf{source}}(k)\left(1 + r_s + 2\sqrt{r_s}\cos(2k\Delta z + \varphi(k))\right) \tag{11}$$

This dispersion must be considered in the processing steps.

But before data can be processed, a calibration must be generated, following a similar procedure to [56]. A mirror is placed in the sample position and an interferogram is acquired. Then, the reference mirror is displaced by 50 μm, and another interferogram

is recorded. A reference spectrum is also recorded with the sample arm blocked. An average of 2000 reference spectra is then subtracted from both interferograms, serving as a background subtraction. Then, the result is normalized by dividing by the averaged reference spectra to effectively numerically flatten the source spectrum.

Next, we take the phase of the Hilbert transform of the signal, which allows us to access the argument of the cosine function in equation (11). Subtracting the result for the first interferogram from the result for the second, the dispersion term $\varphi(k)$ is cancelled and we are then left with just $y_1 \equiv 2k\Delta z_2 - 2k\Delta z_1 = 2k(\Delta z_2 - \Delta z_1) = 2\pi(\Delta z_2 - \Delta z_1)/\lambda$, since the dispersion $\varphi(k)$ does not depend on Δz through air. The function y_1 is then fitted with the sum of a hyperbola (the theoretical wavelength-to-wavenumber conversion) and a third-order polynomial (to partially account for aberrations). We label the fit $\widehat{y_1}$, which is saved for future processing. The k-mapping is performed by interpolating each interferogram on the space defined by $\widehat{y_1}$ using cubic splines. The result is an interferogram linearly sampled in wavenumber.

With the signal now resampled in k, we can tackle the dispersion mismatch with a procedure similar to [54] and [55]. Note that because the wavelength band is so large, slight lens misalignment, and even the coatings on mirrors (if there are more mirrors in one arm than the other), can cause measurable dispersion. Therefore, numerical dispersion compensation is always needed. Taking the phase of the Hilbert transform of the interferogram allows us to access $2k\Delta z + \varphi(k)$, which can be expanded into a Taylor series. The constant term represents an offset, the linear term represents group velocity and $2k\Delta z$, and the higher-order terms represent dispersion. Therefore, a linear fit is subtracted, leaving only quadratic and higher orders. A seventh-order polynomial is then fitted to the data, called $\hat{\varphi}(k)$, which is saved for future processing. The dispersion can then be compensated by multiplying the interferogram by $e^{-i\hat{\varphi}(k)}$.

The remaining step before Fourier transforming is windowing, which can help to reduce side lobes (at the expense of resolution) [57]. We tested several different

windows when processing our data, and found that the best compromise was a compound window of half Blackman, half Hamming, as shown in Figure 16. Because the signal strength is lower for shorter wavelengths, as is apparent Figure 15, the SNR is reduced in this region, with the camera noise affecting the signal considerably in the first 100 pixels. It is thus helpful to weight these wavelengths less heavily in the data processing. Otherwise, we found that there is a significant increase in the noise floor (~7 dB) at 10 klps by using a full Hamming window. Since the visibility is good at longer wavelengths, a Blackman window is unnecessarily severe for the upper portion of the spectrum, and a Hamming window is a good compromise between reducing sidelobes and maintaining axial resolution.

Finally, a fast Fourier transform with 2^{14} points is performed to extract $I_{\mathbf{det}}(\Delta z)$.

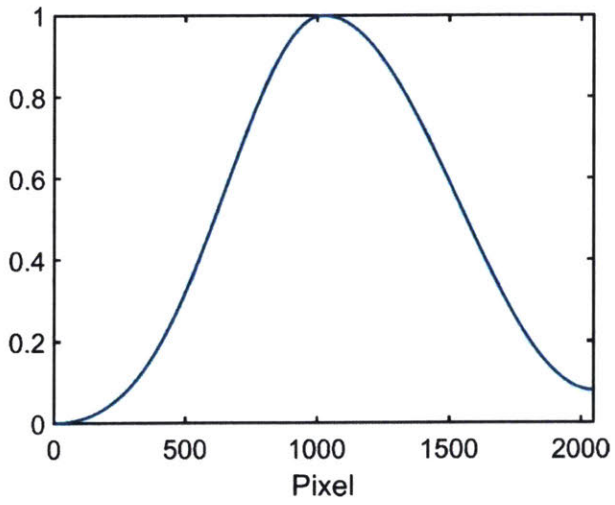

Figure 16: Window used to multiply interpolated and dispersion-compensated interferogram before Fourier transforming

Lastly is z scaling. Instead of just 2 mirror positions for this final calibration step, an interferogram is acquired for each of 7 different mirror positions separated by 50 μm increments. The pixel position of each peak after processing is determined and a linear fit is performed, assuming 50 μm between each peak. This scaling is saved.

With the calibration curves thus obtained, it is possible to process our data by following the steps described above.

Chapter 3

System Characterization

This chapter presents the extensive characterization performed on our system. Furthermore, a summary of our measured system specifications and a comparison with other systems is shown in a table at the end of this chapter. Table 6 below is provided as a reminder, listing the theoretical and simulated specifications of the system.

Table 6: Theoretical and simulated system specifications (reminder)

Axial resolution* in air (μm)	1.8
Lateral resolution* in air (μm)	5/15
Center Wavelength (nm)	1290
A-line rate (klps)	10-146
Imaging range in air (mm)	1.4
Depth of focus in air (μm)	88/790

*Resolution measured as FWHM at focus
Red: configuration 1, blue: configuration 2

3.1 Axial Resolution

By putting a mirror in the sample position, it is possible to measure the system's axial point spread function (PSF), since the mirror acts as a point reflector. By adjusting the delay Δz between the sample and reference mirrors, the axial PSF can be measured for different delays (in other words, different sample depths). The delay was modified by placing the objective and mirror of the reference arm on a 1D translation stage. Interferograms were recorded (at 10 klps, with 25 mW on the sample, with all lenses in place and with the Olympus 5X objective in the sample arm), resulting in the processed 1D data shown in Figure 17.

The resulting axial resolution (FWHM) was 2.0 μm at 89 μm delay and 2.5 μm at 835 μm delay. The signal decays with increasing depth due to finite spectrometer resolution, as will be discussed in the next section.

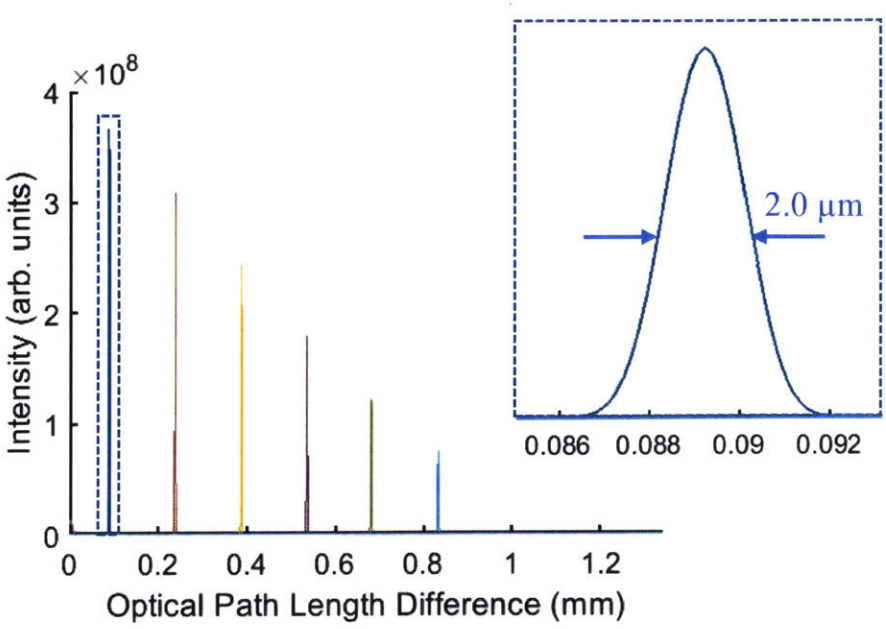

Figure 17: Axial point spread functions (linear scale) for 6 different axial mirror positions

3.2 Sensitivity and Roll-Off

Sensitivity is defined as the smallest signal from a sample that can be detected, relative to the incident power on the sample. To measure sensitivity, a neutral density (ND) filter of known attenuation is placed in the sample arm – in our case, a variable, reflective ND filter set to 25 or 30 dB attenuation – and a mirror is placed in the sample position. The ND filter is used to ensure that the SNR is not limited by the camera's dynamic range. Then, the sensitivity can be calculated from the PSFs: sensitivity = SNR + 2 × 30dB. These measurements were acquired with all lenses in place, in configuration 2 (lateral resolution = 15 μm). Configuration 1 yielded similar results.

Table 7 shows the SNR for 6 different path length differences in a logarithmic scale (at 10 and 146 klps, with 25 mW on the sample). A summary table with the numerical data for the sensitivity is also shown (Table 8). As a reminder, the delay between the sample and reference arms was modified by placing the objective and mirror of the reference arm on a 1D translation stage. 2000 A-lines were incoherently averaged (i.e. power average) to better visualize the noise floor.

Table 7: Experimentally-measured SNR for Olympus and home-built objectives at 10 and 146 klps. 2000 A-lines incoherently averaged for accurate visualization of noise floor.

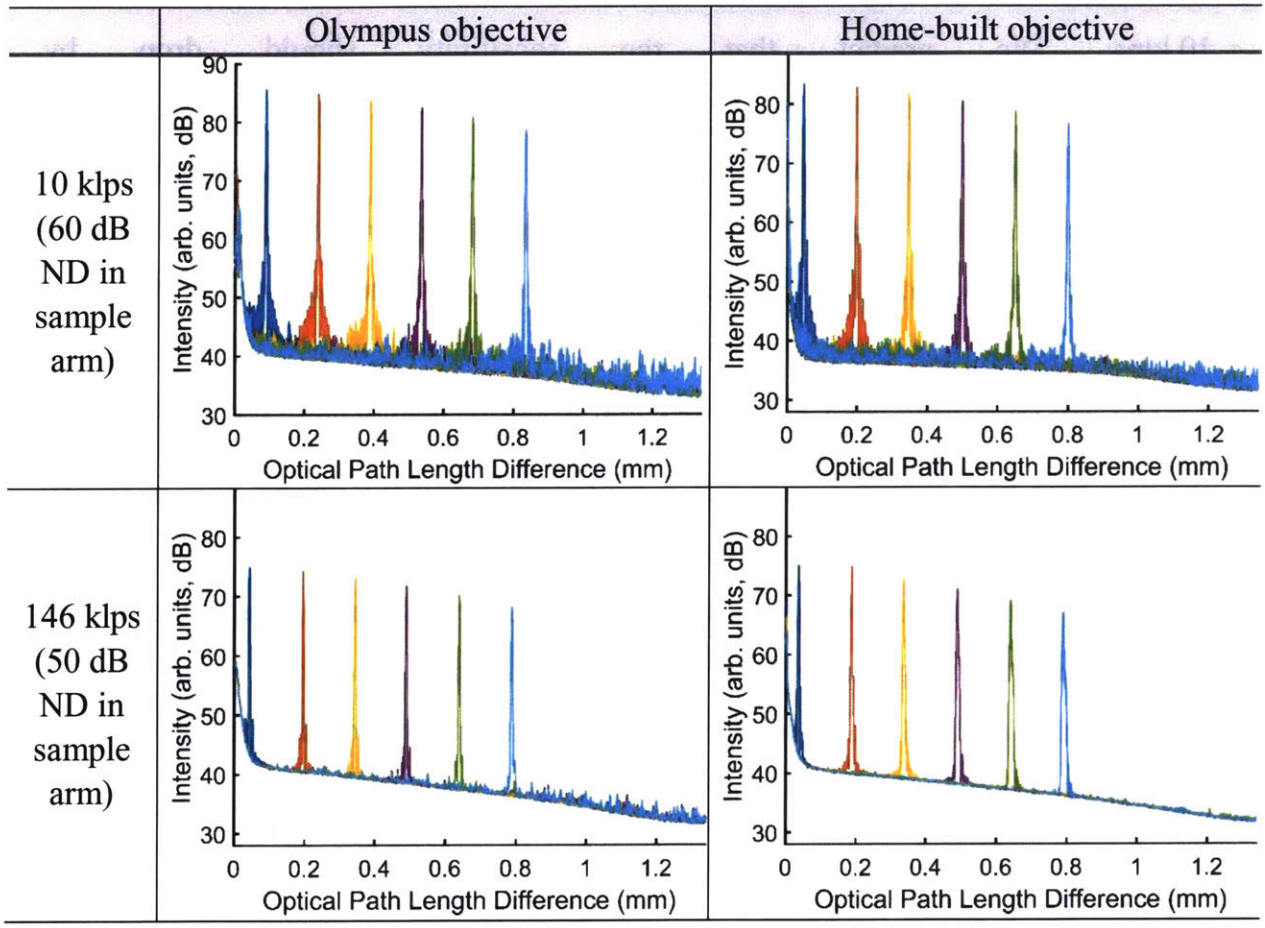

Table 8: Experimentally-measured sensitivity summary for Olympus and home-built objectives at 10 and 146 klps

	Olympus objective	Home-built objective
10 klps (60 dB ND in sample arm)	105 dB	107 dB
146 klps (50 dB ND in sample arm)	84 dB	84 dB

The sensitivity at 146 klps is lower than expected compared with the sensitivity at 10 klps. We predict that the sensitivity should drop by $10\log_{10}(146\text{klps}/10\text{klps}) = 12$ dB. However, the observed decrease in sensitivity is 21-23 dB. This can partially be explained by an increase in camera noise at higher speeds. Furthermore, laser RIN has a larger effect at higher speeds, since a longer camera integration time effectively averages out some laser noise. We therefore note that lower-noise supercontinuum sources have recently been developed (e.g. SuperK EXTREME OCT from NKT Photonics), and would be beneficial to our application.

We also note from Figure 17 and Table 7 that signal intensity decays with increased optical path length difference, but so does the background. To observe the true SNR, we can to perform our processing steps on a reference spectrum, then subtract this processed reference spectrum from the PSF data. This allows for a more accurate representation of the SNR decay, as shown in Figure 18 for the Olympus objective in the sample arm, recorded at 10 klps.

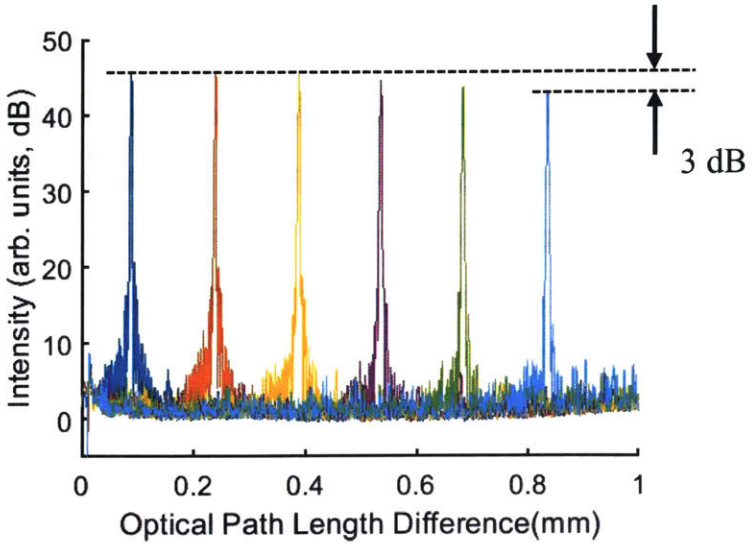

Figure 18: Experimentally-measured SNR data with Olympus objective, at 10 klps, with subtracted baseline, log scale

Figure 19 shows the drop in SNR with sample depth in linear scale, which has the same shape at 10 and 146 klps and for both objectives. This decay, called roll-off $R(\Delta z)$, is due to finite spectrometer resolution, and is well-known in OCT systems. It is theoretically expressed by [58]:

$$R(\Delta z) = \mathrm{sinc}^2\left(\frac{\pi \Delta z}{2d}\right) \exp\left(-\frac{\pi^2 w^2 (\Delta z)^2}{8d^2 \ln(2)}\right) \tag{12}$$

with $w = \delta\lambda/\Delta\lambda$, $d = \lambda_0^2/(4\Delta\lambda)$, where $\Delta\lambda$ is the wavelength spacing between pixels, $\delta\lambda$ is the spectrometer resolution λ_0 is the center wavelength.

To calculate $\delta\lambda$, we look at a diffraction-limited spot produced on the camera by a single wavelength λ_1, and determine the wavelength λ_2 that would be one spot FWHM away on the camera. $\delta\lambda = \lambda_2 - \lambda_1$ is termed the spectrometer resolution. Our design, described in chapter 2, aimed to match $\delta\lambda$ to $\Delta\lambda$, where one $1/e^2$ spot size diameter on the camera would equal the size of a pixel (10 μm). The theoretical w for our system is therefore $w = 1$. With this value and the other parameters of our system, our results do not match the predicted roll-off curve. However, with a fitted w of 1.47, the real roll-off matches with the theoretical roll-off quite well.

That the actual w is larger than the theoretical w is not surprising. Though great care was taken when aligning the spectrometer, small offsets can lead to a non-negligible increase in spot size, increasing $\delta\lambda$, and thus w. For example, a 1° tilt in x of the achromat can double the spot size in y on the camera. (This is the most sensitive degree of freedom, and tilting or decentering other elements does not affect the spot size as much.)

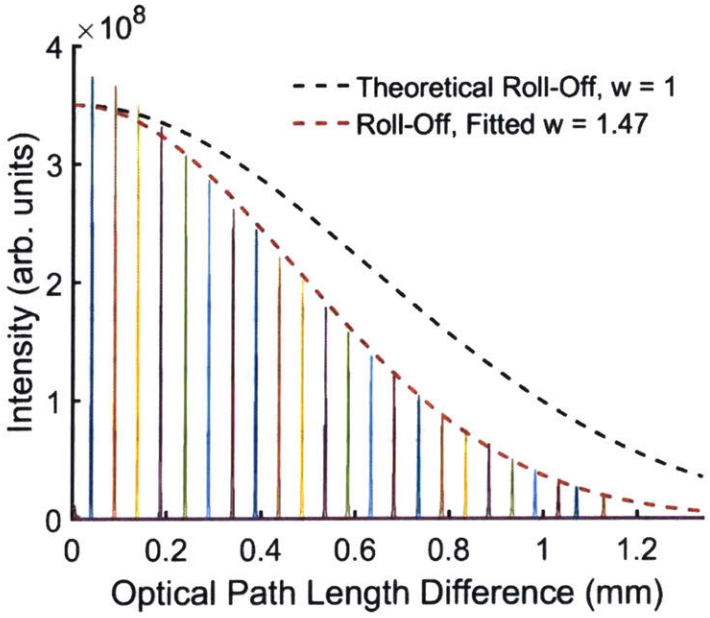

Figure 19: Experimentally-measured SNR data with Olympus objective, at 10 klps, linear scale, and roll-off curves

3.3 Lateral Resolution

The lateral resolution was measured with a USAF 1951 target. In configuration 2, with scan and tube lenses of f = 100 mm and using the Olympus 5X objective, the smallest set of distinguishable lines is in group 4, element 6. This can be seen in Figure 20, an *en face* OCT image of the target and Figure 21, a single line and single column from that image. Thus, the largest element that cannot be observed (group 5, element 1) corresponds to 32.00 line pairs/mm, and an approximate lateral resolution of 15.6 μm, as expected. The reader may note that the 6 in the bottom left of Figure 20 looks clearer than the 5 in the top right. This may be due to aberrations, and it should

be kept in mind while imaging that certain lateral regions may be more aberrated than others.

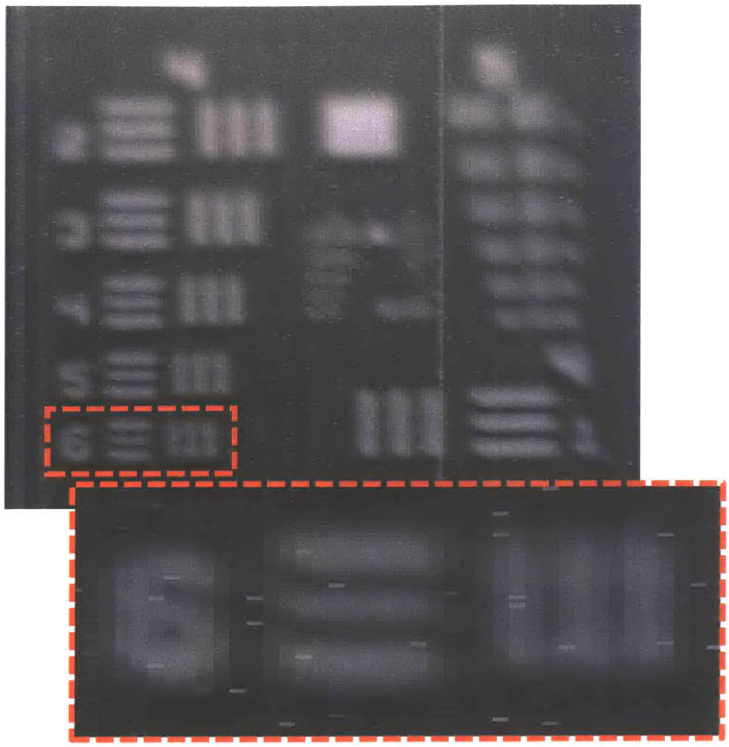

Figure 20: En face *OCT image (summed axial intensity) of center of USAF 1951 resolution target (configuration 2 with scan and tube lenses of f = 100 mm, Olympus 5X for focusing)*

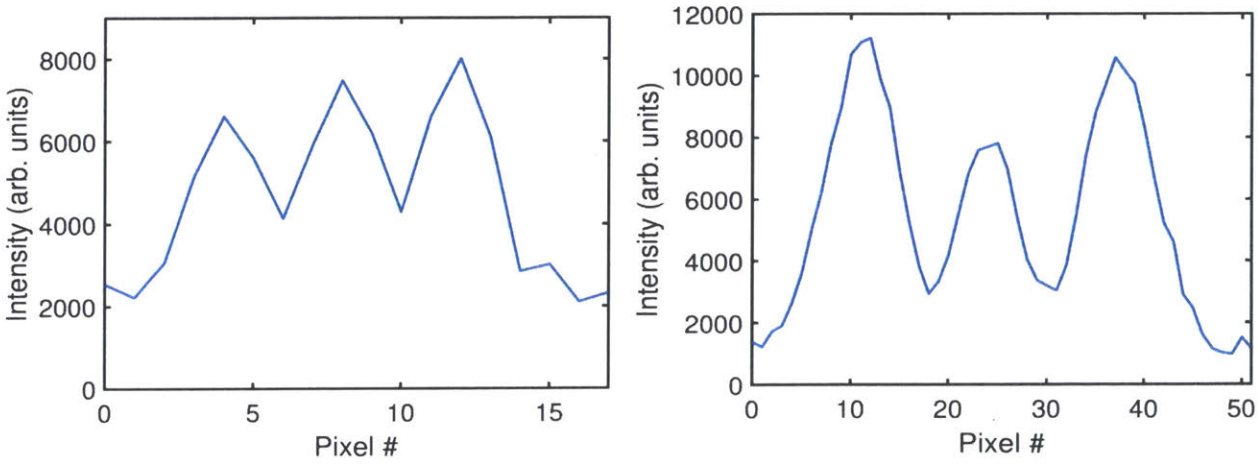

Figure 21: Left/right is single line/column from the en face *OCT image of a USAF 1951 resolution target, group 4, element 6 vertical/horizontal bands in configuration 2 using Olympus objective*

The same target was imaged with our home-built objective used to focus light onto the sample. The results are shown in Figure 22 and Figure 23, with an approximate lateral resolution of 13.9 μm, close to the expected values from simulation.

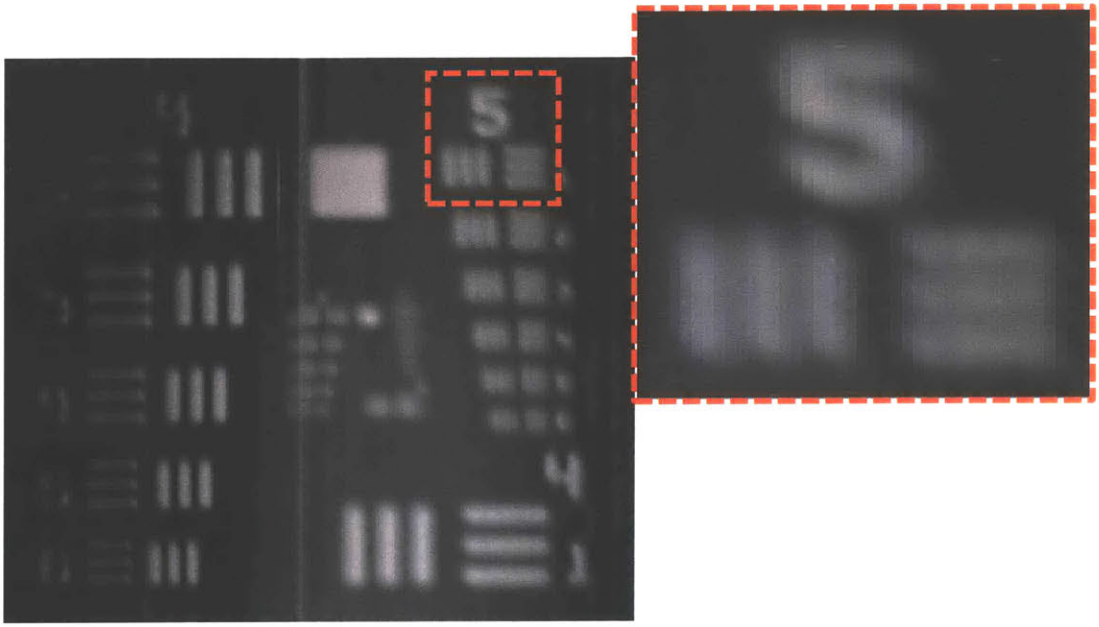

Figure 22: En face OCT image (summed axial intensity) of center of USAF 1951 resolution target (configuration 2 with scan and tube lenses of f = 100 mm, home-built objective for focusing)

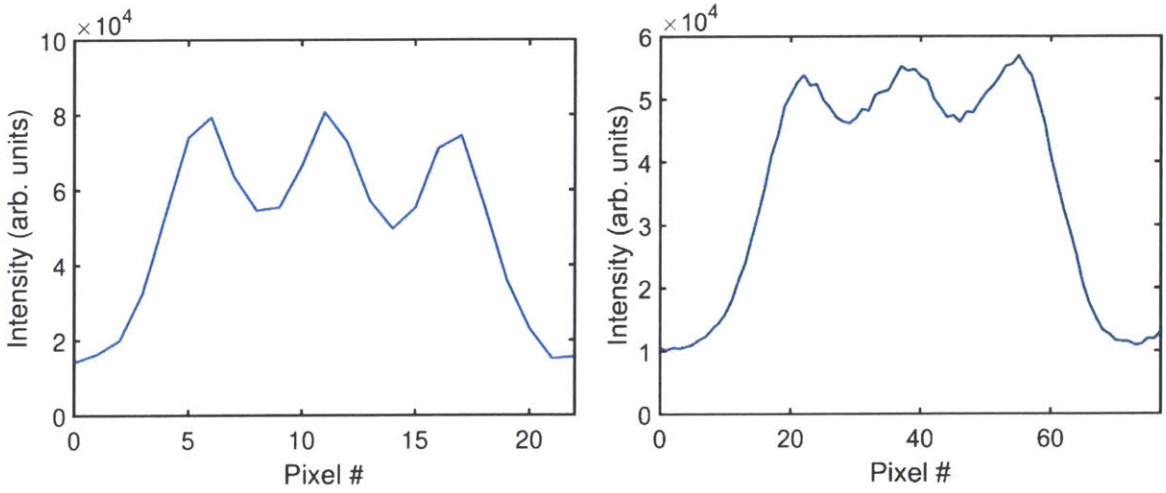

Figure 23: Left/right is single line/column from the en face *OCT image of a USAF 1951 resolution target, group 5, element 1 vertical/horizontal bands in configuration 2 using home-built objective*

In configuration 1 (tube lens of $f = 300$ mm), the last element with distinguishable lines is (6,4) for both the Olympus and home-built objectives, as shown in Figures 27 through 30. This implies a lateral resolution of 4.9 μm, as expected, though once again, the images suggest that we may want investigate field curvature, as certain regions appear more in-focus than others.

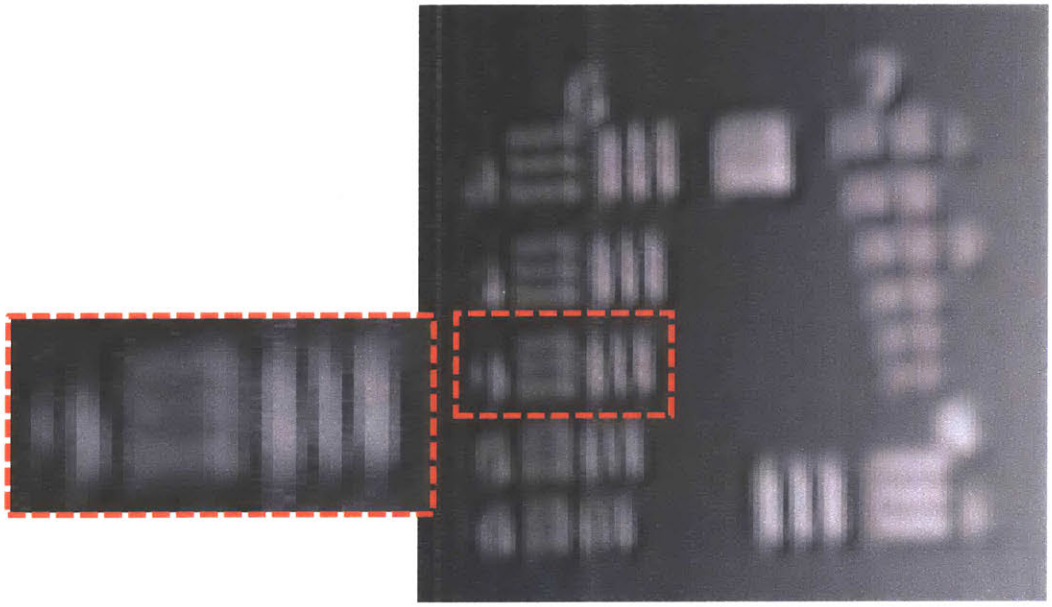

Figure 24: En face OCT image (summed axial intensity) of center of USAF 1951 resolution target (configuration 1 with tube lens of $f = 300$ mm, Olympus 5X for focusing)

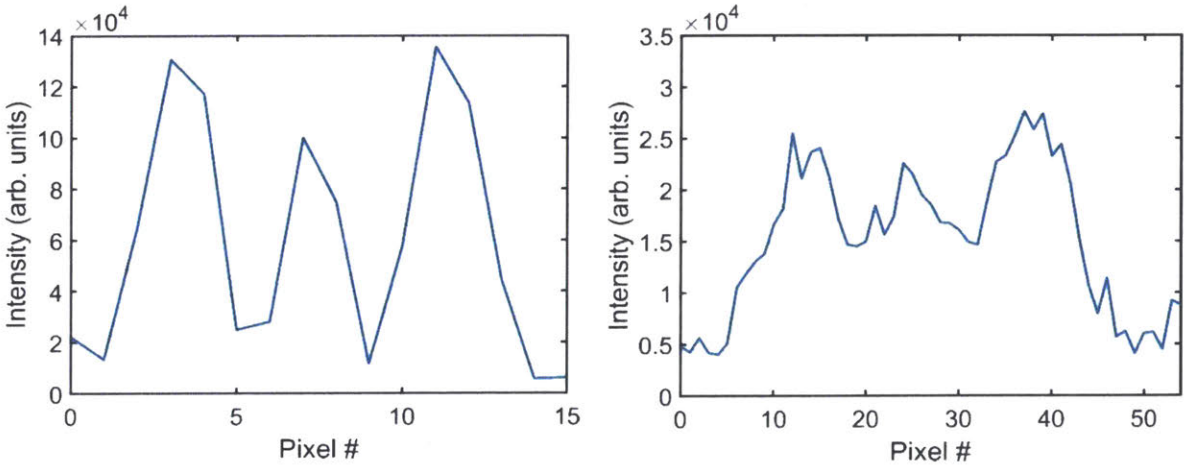

Figure 25: Left/right is single line/column from the en face OCT image of a USAF 1951 resolution target, group 6, element 4 vertical/horizontal bands in configuration 1 using Olympus objective

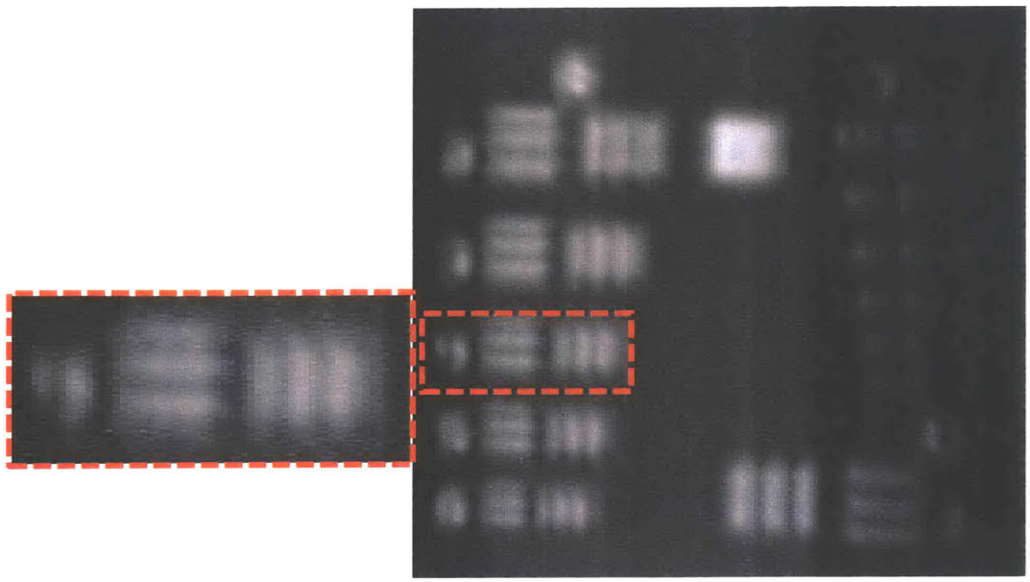

Figure 26: En face OCT image (summed axial intensity) of center of USAF 1951 resolution target (configuration 1 with tube lens of f = 300 mm, home-built objective for focusing)

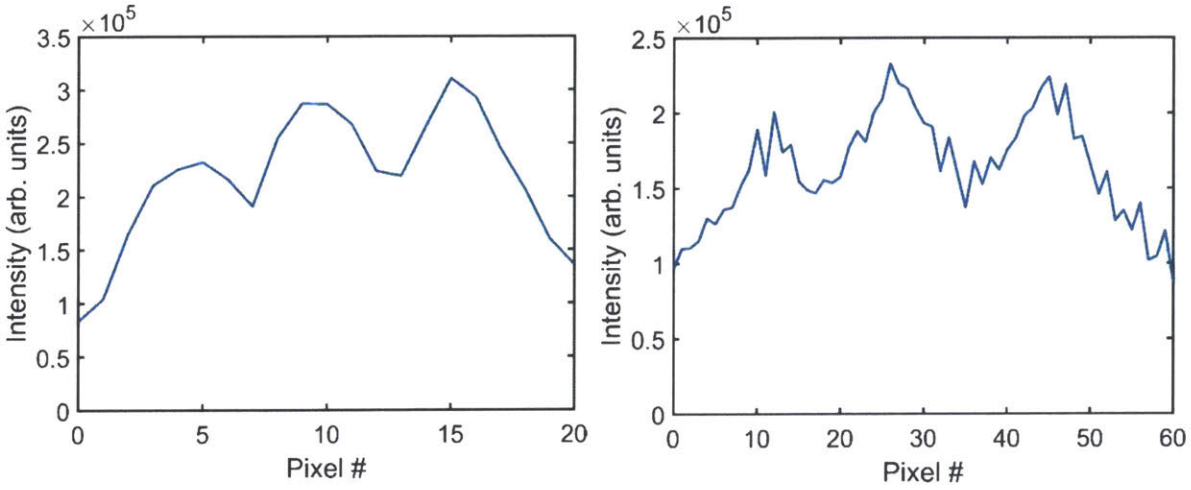

Figure 27: Left/right is single line/column from the en face OCT image of a USAF 1951 resolution target, group 6, element 4 vertical/horizontal bands in configuration 1 using home-built objective

The lateral field of view (FOV) was measured by translating a razor blade by known increments for different voltages applied to the galvo mirrors. Then, a linear fit could be applied to determine the scaling between volts and micrometer beam translation on the sample. In the configuration 2 (scan and tube lenses of f = 100 mm), the lateral

FOV was roughly 6 mm × 6 mm for the Olympus objective before clipping or major distortion occurred. For the home-built objective in configuration 2, the lateral FOV was smaller (roughly 3.5 mm × 3.5 mm). In configuration 1 (tube lens of f = 300 mm), the lateral FOV was roughly 1.8 × 1.8 mm for the Olympus objective and 1.2 × 1.2 mm for the home-built objective.

3.5 Summary of System Specifications and Comparison with Commercial NIR OCT and Shorter Wavelength UHR-OCT

Table 9: Experimentally-measured system specifications (in 2 different configurations) and comparison

	Liu et al. Micro-OCT [9]	Commercial High-Res. NIR SD-OCT [17]	Our system
Axial resolution[(a)] in air (μm)	1.4	5.5	2.0
Lateral resolution[(a)] in air (μm)	2.8	4.1-12	5/15
Center Wavelength (nm)	800	1300	1290
A-line rate (klps)	16	10-146	10-146
Relative Penetration	Shallow	Deep	Deep
Imaging range in air (mm)	0.64	3.5	1.4
Optical power at sample (mW)	10	3.5	25
Reflection sensitivity at Δz=0 (dB)	Not reported	109[(b)]	105[(b)]

[(a)]Resolution measured as FWHM at focus

[(b)]Measured at 10klps

Table 9 presents a summary of the system specifications, as well as a comparison with a shorter-wavelength UHR-OCT system and a commercial system with a center wavelength of 1300 nm. We note that the measured specifications of our system match the theoretical predictions well.

Chapter 4

Imaging Results

4.1 Scotch Tape

In order to obtain a visual understanding of our system's performance, a roll of Scotch tape was imaged using both our system and a standard swept-source OCT (SS-OCT) system. The standard OCT system had axial and lateral resolutions of roughly 15 μm and 30 μm, respectively, with an imaging speed of 45 klps, and was centered at 1300 nm. For this comparison, our system was used in configuration 2 (lateral resolution of 15 μm), with the Olympus objective and with an imaging speed of 10 klps. In Figure 28, the high axial resolution of our system is clearly visible, with sharp contrast between the different layers of tape, as compared with the standard OCT system, where they are blurred. Note that for all the images in this chapter, the color bar was empirically adjusted to optimize contrast, with black to white spanning roughly 30-40 dB. Also, the height of the images represents the axial (in-depth) dimension, and the width represents the lateral dimension.

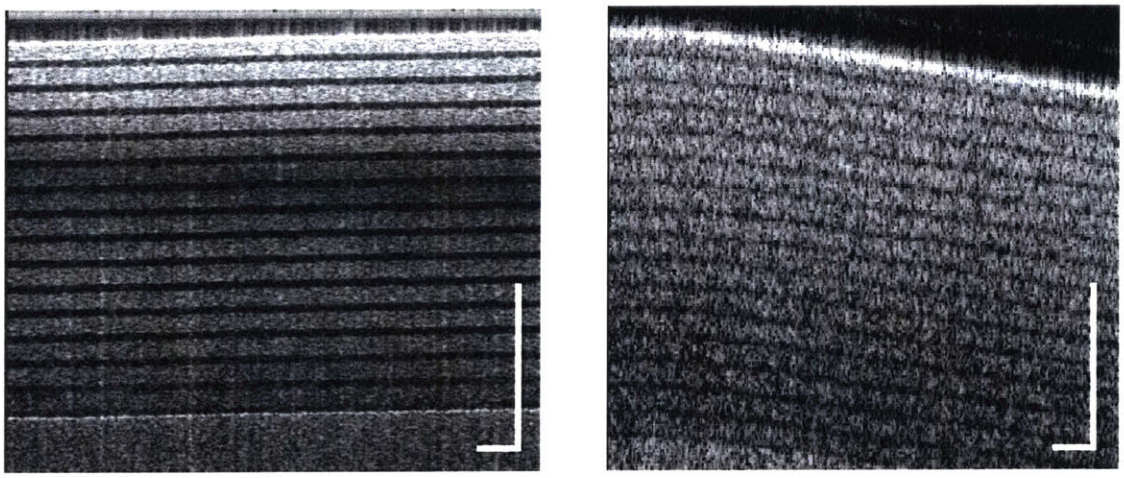

Figure 28: Comparison of single B-scan of Scotch tape imaged with our UHR-OCT system with Olympus objective, 10klps (left) versus a standard OCT system (right). Scale bars: 500 μm.

We also used Scotch tape to visually characterize our system and investigate further processing. We imaged at 10 klps, then at 146 klps with both the Olympus objective and the home-built objective. We started with configuration 2 (lateral resolution of 15 μm, Figure 29 and Figure 30), and then imaged in configuration 1 (lateral resolution of 5 μm, Figure 31).

In the left panels of Figures 29 to 31, a single B-scan is shown with the processing described in chapter 2. Also, the autocorrelation signal (i.e. the signal acquired with the reference arm blocked) was subtracted. In the right panels, we performed further processing: binning of 5 A-lines and subtraction of the shape of the signal decay, i.e. a piecewise linear fit of the averaged A-lines.

At 10 klps, there is enough SNR to see all 15 layers of tape, plus the plastic base underneath. There is not a tremendous difference between the Olympus objective and our inexpensive home-built objective made of 3 standard lenses when the back aperture is underfilled, as is the case in configuration 2. Therefore, the home-built objective is a reasonable low-cost alternative for low N.A. applications. We did, however, notice some field curvature from the home-built objective and aberrations from ghosting due to reflections between lenses in the objective. At 146 klps, layers 6 to 15 of the tape only become visible after binning A-lines, thereby reducing the effective A-line rate.

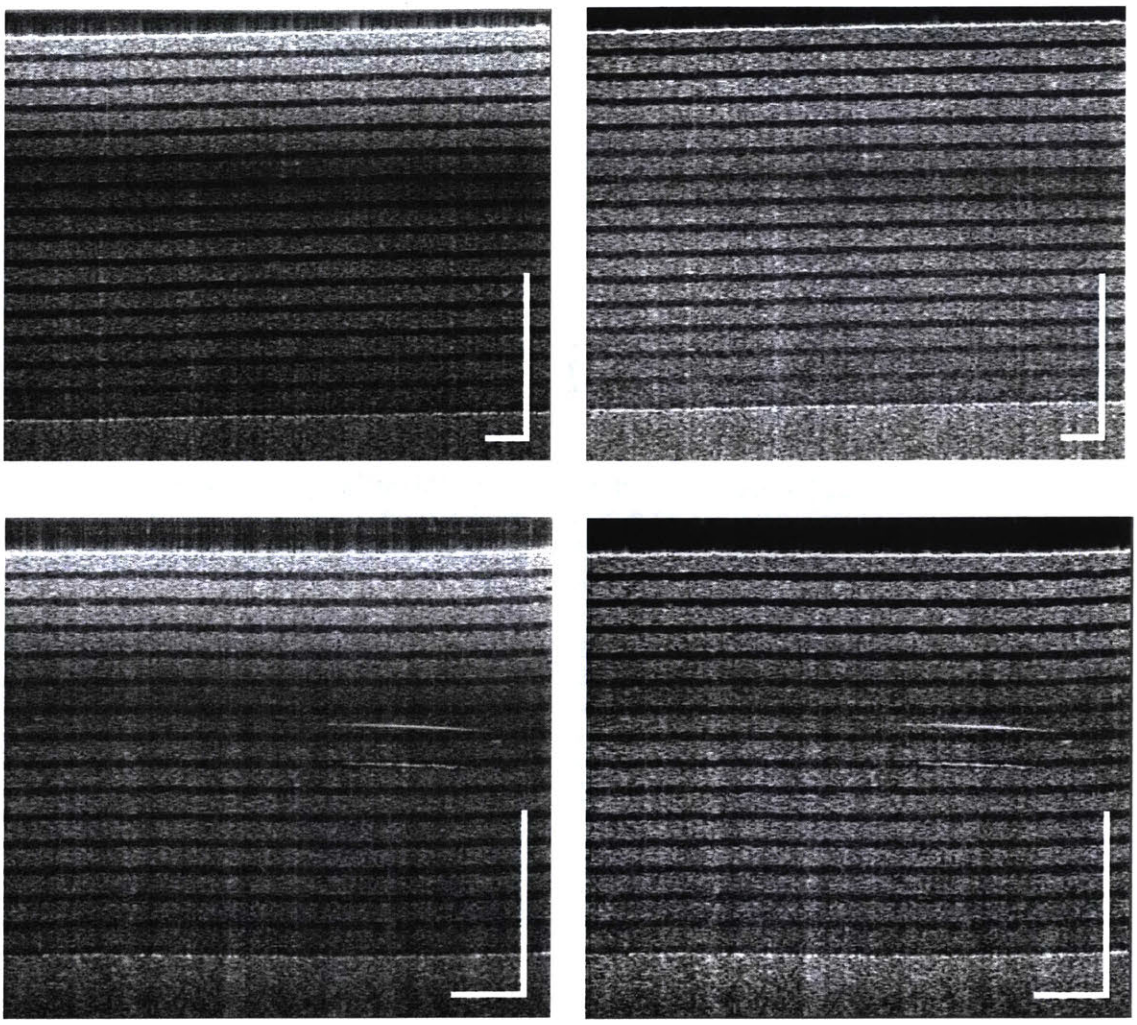

Figure 29: Scotch tape imaged with Olympus objective (top row) and home-built objective (bottom row) at 10 klps in configuration 2. Left: standard processing plus subtraction of autocorrelation. Right: standard processing plus subtraction of autocorrelation and additional steps (binning of 5 A-lines, subtraction of fitted signal decay). Scale bars: 500 μm.

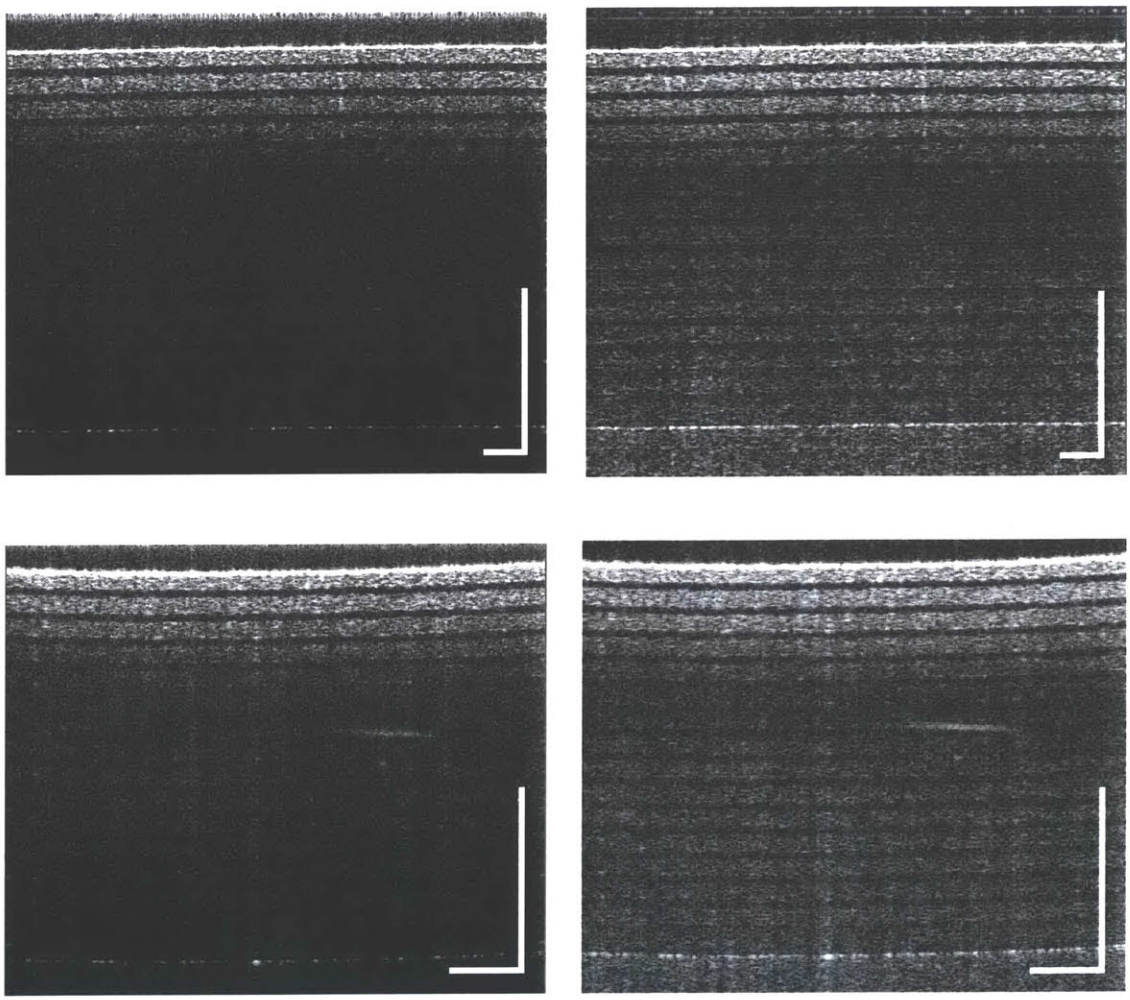

Figure 30: Scotch tape imaged with Olympus objective (top row) and home-built objective (bottom row) at 146 klps in configuration 2. Left: standard processing plus subtraction of autocorrelation. Right: standard processing plus subtraction of autocorrelation and additional steps (binning of 5 A-lines, subtraction of fitted signal decay). Scale bars: 500 μm.

As mentioned above, the tape was also imaged in configuration 1, with a tube lens of $f = 300$ mm and a lateral resolution of 5 μm (Figure 31). The speckle size is smaller, evidence of the better lateral resolution (note the lateral scale bar), and the sensitivity falls off at a smaller axial distance. We expect the axial depth of focus to be significantly reduced, and thus the axial field of view to be greatly reduced. Despite this, it was still possible to see all 15 layers of tape at 10 klps.

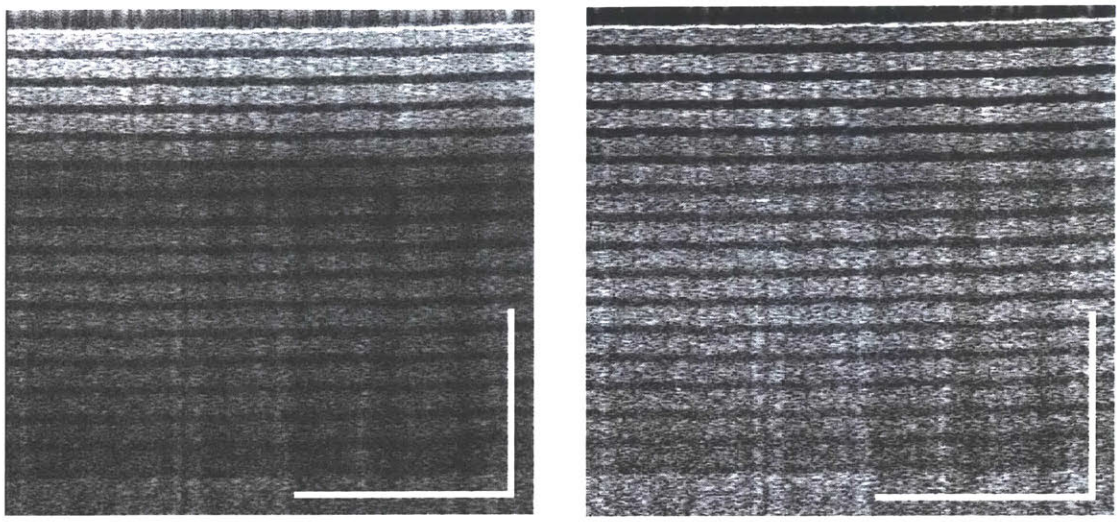

Figure 31: Scotch tape imaged with Olympus objective at 10 klps in configuration 1. Left: standard processing plus subtraction of autocorrelation. Right: additional processing, as described above. Scale bars: 500 μm.

4.2 Cardiology: Toward Intraoperative Visualization of Conduction Tissue

The larger working distance of the Olympus objective (23 mm) over our home-built objective (4 mm) makes it more practical to image biological samples. Thus, the Olympus objective was used to image the heart. Furthermore, in this exploratory study, we wanted to have a large field of view. Therefore, the system was used in configuration 2 (lateral resolution of 15 μm). The A-line rate was 10 klps, with 2000 A-lines per image, and binning of 3 A-lines (reducing the effective A-line rate to 3.3 klps) was performed.

As an initial study investigating the electrical conduction system of the heart, we imaged the left bundle branch of two freshly-excised porcine hearts, a common model for the human heart [59]. We first found the membranous septum in the left ventricle near the mitral valve by trans-illumination. We then imaged this area, with the results shown in Figure 32. There were not many features visible in this region; only the endocardium could be distinguished, as expected.

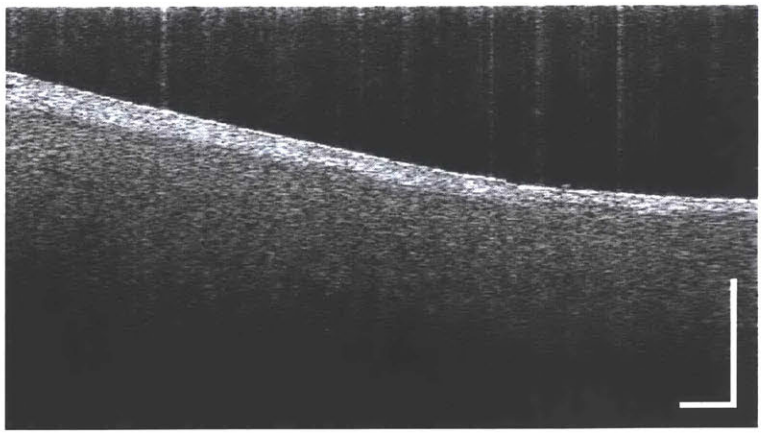

Figure 32: Membranous septum (left ventricle near mitral valve) of porcine heart. Scale bars: 300 μm.

We then displaced the sample on a translation stage and found a blood vessel, which can be seen in Figure 33.

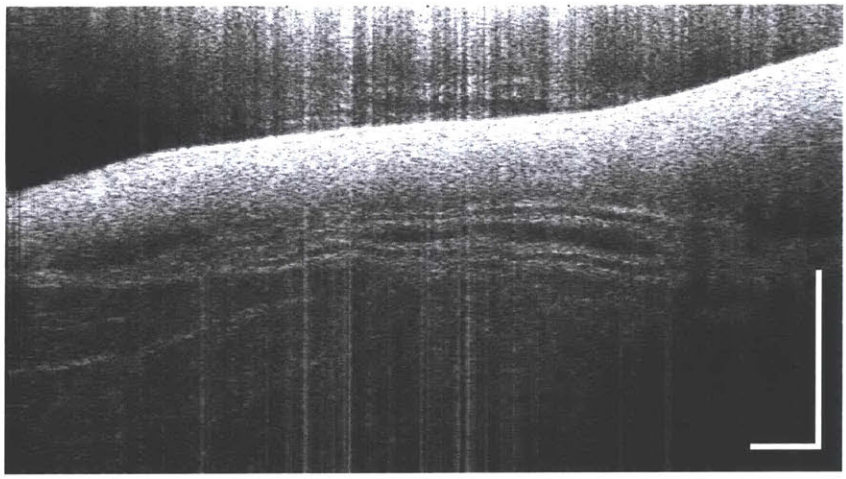

Figure 33: Blood vessel in left ventricular septal wall. Scale bars: 500 μm.

Moving the sample on a translation stage such that we imaged further from the membranous septum, conduction tissues began to appear (Figure 34). 3D volumes were then acquired, rendered in Figure 35 (using ImageJ). The left bundle branch was also imaged in a second pig heart. We obtained similar results to the ones shown above, albeit with slightly more densely-packed fibers (Figure 36). A histology slide (dyed with Masson's trichrome) is shown in Figure 37 for reference, where

conduction fibers of the left bundle branch of the porcine heart are visible. The structures seen in histology are very similar to those acquired by our UHR-OCT.

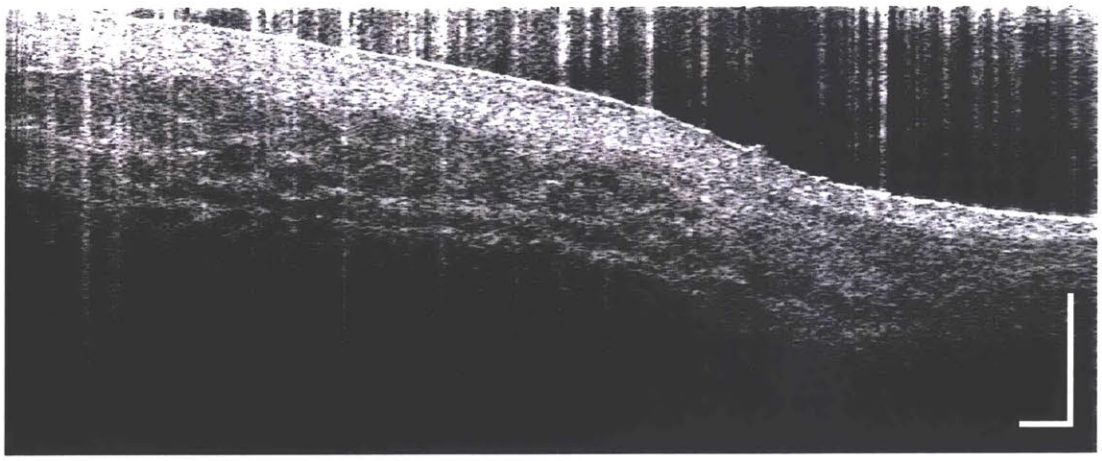

Figure 34: Transition from membranous septum to conduction tissue in left bundle branch, porcine heart. Scale bars: 300 μm.

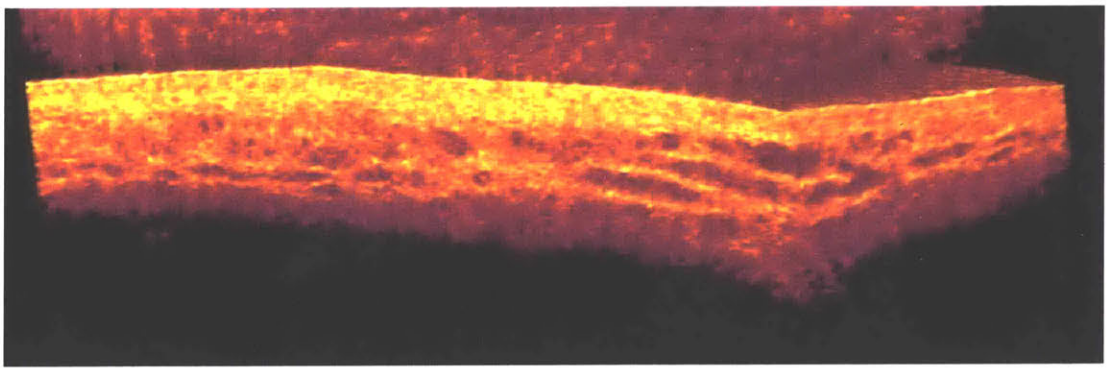

Figure 35: 3D volume of left bundle branch conducting fibers. Rendered in ImageJ.

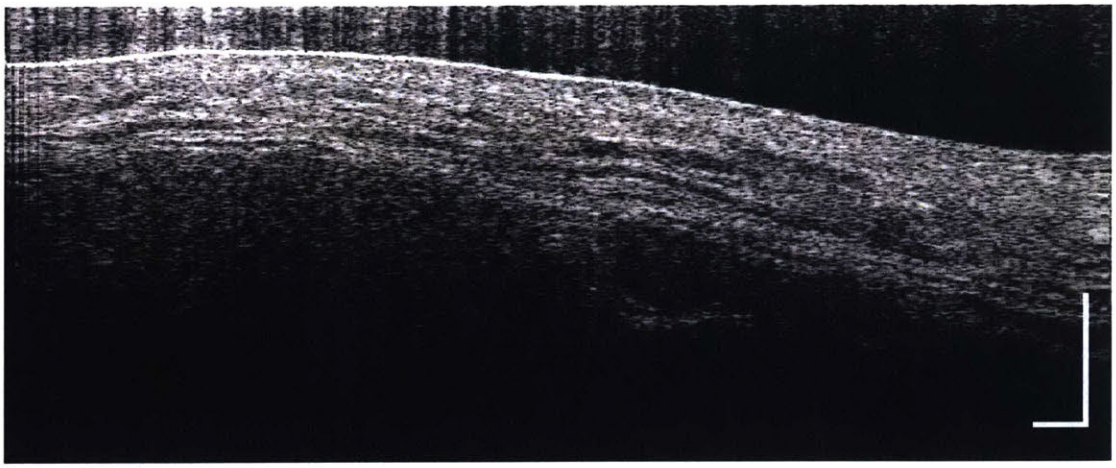

Figure 36: Conduction tissue in left bundle branch, second porcine heart. Scale bars: 300 μm.

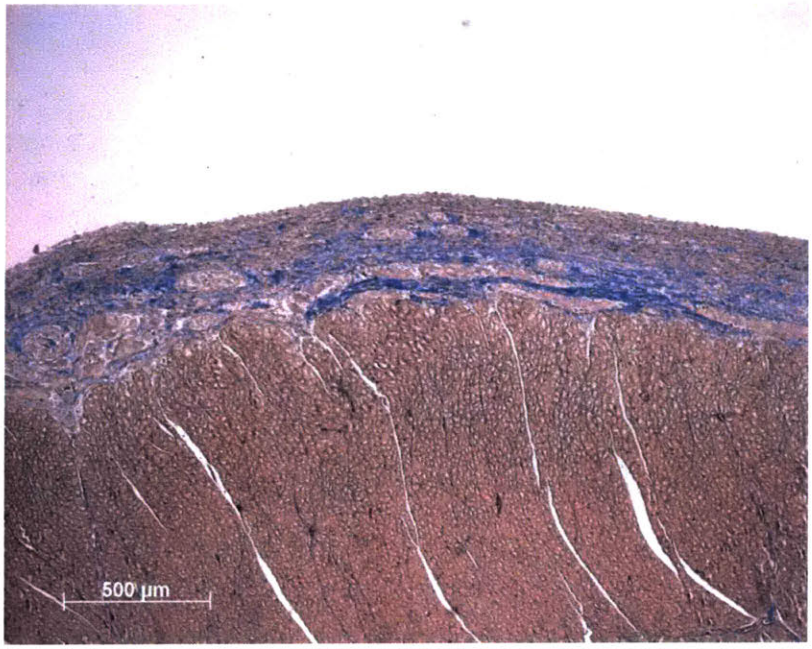

Figure 37: Histology slide (dyed with Masson's trichrome) of left bundle branch in porcine heart. Light pink: conducting fibers in the left bundle branch; blue: collagen; dark pink: muscle. Image courtesy of Dr. Vera Aiello, Laboratory of Pathology, Heart Institute (InCor), University of São Paulo Medical School, Brazil.

We also compared our images to those obtained with a standard SS-OCT system centered at 1300 nm, with axial and lateral resolutions of approximately 15 μm and 30 μm, respectively (Figure 38). The endocardium was pierced with a needle to ensure that we imaged the same region with both systems. For the bundles surrounding the needle point, the conduction tissue can be seen with some imagination in the standard OCT system, but it is not easily observable. This is logical, since these conducting fibers are roughly 50 μm wide (axially) or smaller. Therefore, it is difficult to observe them with an axial resolution of 15 μm.

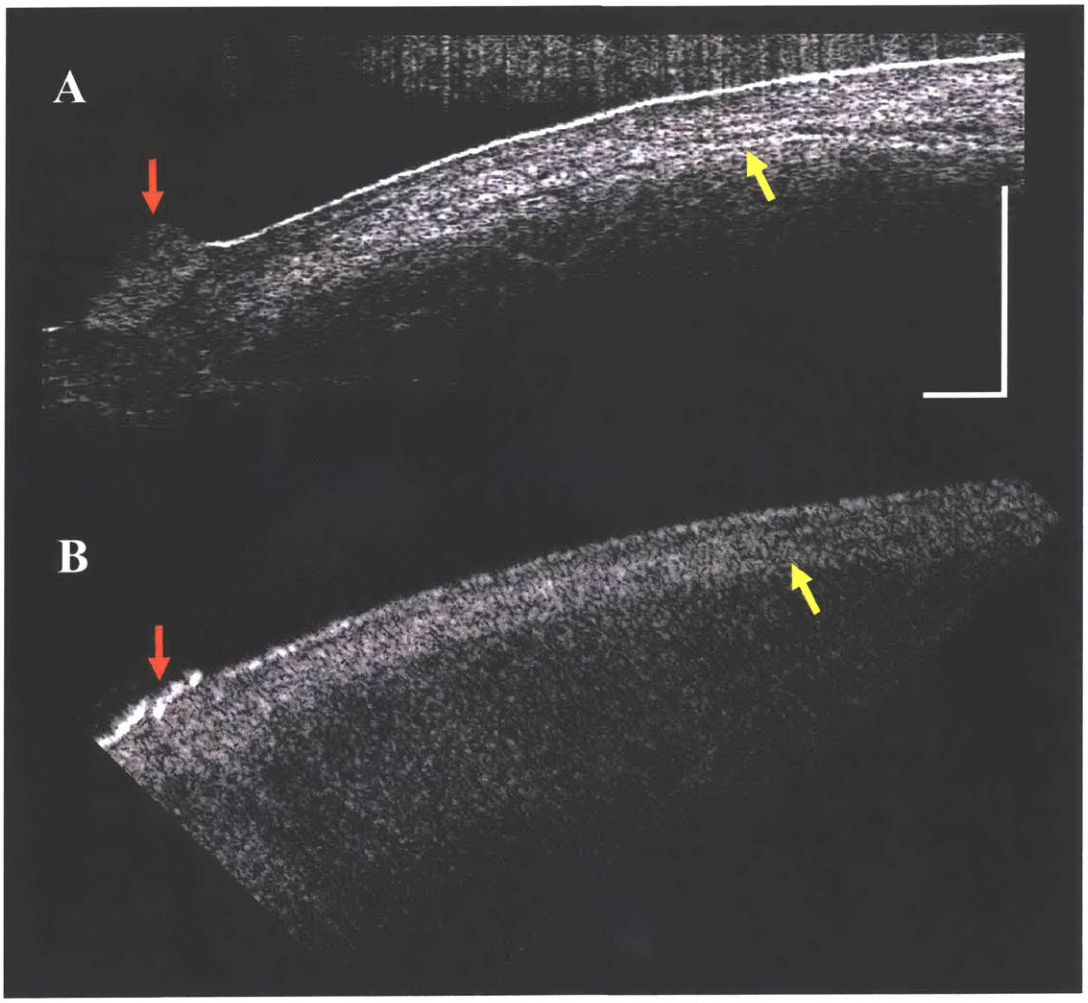

Figure 38: Comparison between conduction tissue in left bundle branch imaged with our system (A) versus standard OCT system (B).
Red arrows indicate tissue pierced by needle. Yellow arrows indicate conduction tissue (dark) surrounded by highly-scattering collagen (bright) Scale bars: 500 μm.

4.3 Inner Ear

We attempted to image through the cochlear bone of a gerbil (a few hours after the animal was sacrificed). However, the tectorial membrane and basilar membrane appeared blurred, and we could not visualize hair cells. We think this might be due to poor sample placement, as we found it difficult to align the gerbil ear with our optical system. Alternatively, perhaps the beam became too distorted as it traveled through the cochlear bone, and this induced aberrations, degrading resolution. We will try to image a gerbil ear again to see if we can obtain clearer images with better placement of the gerbil head.

4.4 Ophthalmology: Seeing Deeper with UHR into Sclera and Limbus

We used our system to image freshly-excised porcine eyeballs, first investigating the cornea, then the scleral and limbal regions.

4.4.1 Cornea

The cornea was imaged in configuration 1 (resolution of 5 μm × 5 μm × 2 μm), at an A-line rate of 10 klps, with 2000 A-lines per image and binning of 3 A-lines (reducing the effective A-line rate to 3.3 klps). With our resolution, nerves were visible in the focal plane of the objective, and we could follow their trajectory from their base in the limbus extending out into the cornea (Figure 39).

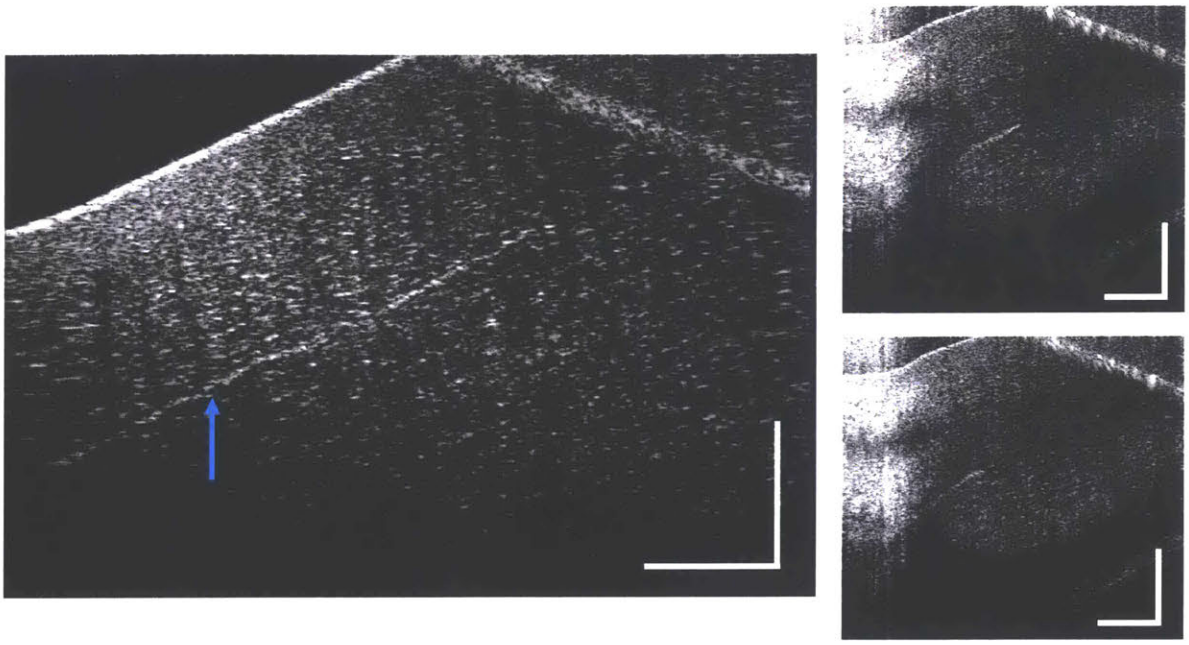

Figure 39: Cornea of freshly-excised porcine eyeball. The highly scattering tissue is most likely a corneal nerve bundle (blue arrow). The right panels show that the nerve bundle can be followed back to the limbus. Some image wrapping occurs at the top right of the image, where negative delays appear folded over. Scale bars: 300 μm.

4.4.2 Sclera/Limbus

As mentioned in chapter 1, the sclera and limbus have been recent regions of interest in OCT imaging. Our deep-penetration UHR-OCT system can be used to clearly observe the features in the corneo-sclera angle, as shown in Figure 40. Furthermore, our system can be used to image deeper into the sclera, where features such as blood vessels are easily identifiable (Figure 41 and Figure 42). This leads us to believe that our system could be used to diagnose pathologies in the sclera. This region was imaged in configuration 2 (resolution of 15 μm × 15 μm × 2 μm), at an A-line rate of 10 klps, 2000 A-lines per image, and binning of 3 A-lines (reducing the effective A-line rate to 3.3 klps).

Figure 40: Corneo-scleral angle of freshly-excised porcine eyeball. Scale bars: 500 μm.

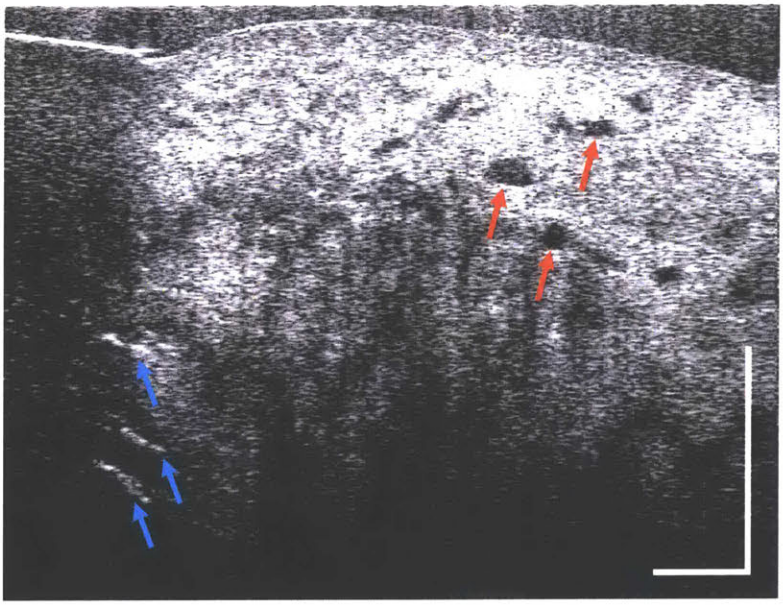

Figure 41: Limbus and sclera of freshly-excised porcine eyeball. Red arrows: blood vessels. Blue arrows: corneal nerves. Scale bars: 500 μm.

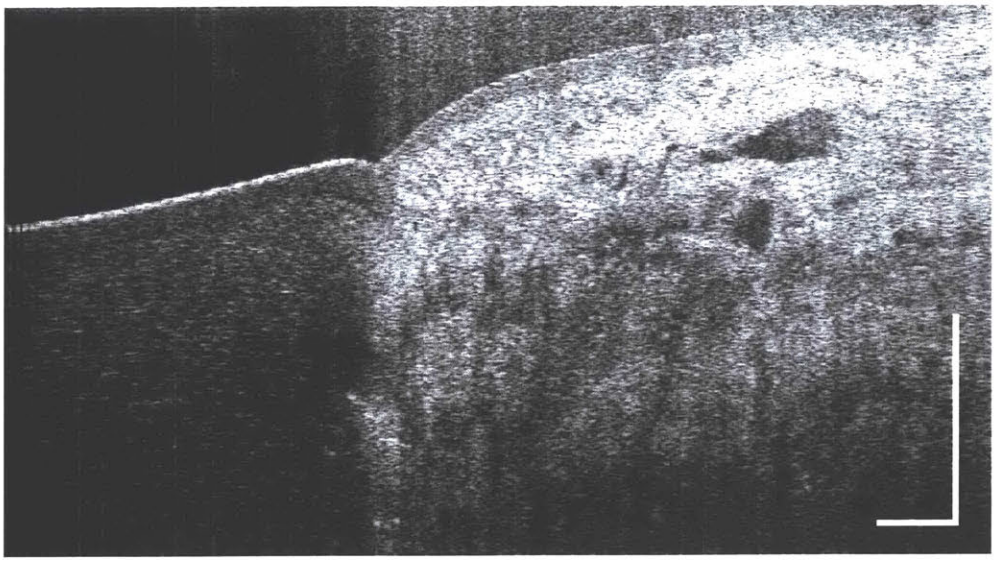

Figure 42: Limbus and sclera of freshly-excised porcine eyeball. Scale bars: 500 μm.

Chapter 5

Outlook

5.1 Future Projects and Improvements

As evidenced by our scleral and limbal images, our system would be improved by eliminating the complex conjugate artifact induced by positive and negative delays $\pm\Delta z$ overlapping. A simple modification could be, as described in [20], to put the reference mirror on a piezoelectric stack, allowing us to acquire the complex conjugate of the signal with very small axial displacement of the reference mirror. The ambiguity between positive and negative delays is then lifted, and there is no longer an overlaid flipped image when imaging deep in tissue. This would allow us to image as deeply as we want over a field of view limited by the axial DOF (until the maximum tissue penetration depth is reached, after which the signal is absorbed or multiply scattered in the sample).

Furthermore, we could extend the axial DOF by engineering the PSF on the sample. This would be especially beneficial in our higher lateral resolution case (configuration 1, lateral resolution of 5 μm). For example, we could employ a quasi-Bessel beam instead of a Gaussian beam, as in [9], which increases the DOF without sacrificing resolution. We may see a drop in sensitivity with this technique, since more power is distributed in the sidelobes of a Bessel beam, but we will likely find it to be a worthwhile compromise at low imaging speeds. Other possible approaches exist, such as using a synthetic aperture, as in [60].

Another improvement could be to perform spectral shaping at the source output. As explained in section 2.4, we numerically window out some of our shorter-wavelength signal since there is lower SNR in that region. However, we could choose to replace the 10 dB neutral density filter that is directly at the output of the laser with a filter permitting shorter wavelengths to pass and attenuating longer wavelengths. This

would allow us to truly use our whole wavelength band, improving axial resolution and sensitivity.

We also plan to use our system to perform vibrography, which has previously been realized in our laboratory [61]. We will have to characterize, and likely improve, the phase stability of our system, notably by using smaller and more stable galvo mirrors to scan the beam on the sample. Vibrography will be critical when performing any studies of the ear, since we hope to learn more about the mechanisms of sound transmission.

In terms of studies in the near future, we plan to pursue imaging of the conduction system of the heart. We will image additional porcine hearts to map out more of the conduction system, including the AV node, and send these specimens to histology for direct confirmation of our findings. We also plan to image human hearts with congenital heart defects, in order to test whether we can non-invasively visualize abnormal conduction systems, or conduction systems in abnormally-formed hearts. We will also investigate the polarization-dependence of the images (in fact, it would be useful to add polarization sensitivity to the system since the specialized conduction fibers are structured, and are surrounded by collagen, which is birefringent). This will be a proof-of-concept for intraoperative guidance for surgeons repairing congenital heart defects. The system will also likely be useful to cardiac pathologists, who may be able to use it to study the conduction system of intact heart specimens.

Lastly, we plan to investigate the possibility of using our UHR-OCT system to characterize silicon devices such as photovoltaic cells. Because these structures contain micrometer-sized layers of high refractive index, and are transparent to infrared wavelengths, our system may be ideally suited for this application.

5.2 Conclusion

We have demonstrated an ultrahigh-resolution, deep-penetration spectral-domain OCT system centered at 1290 nm with a 2 μm axial resolution and a 5-15 μm lateral

resolution, with imaging speeds from 10 to 146 klps. This is, to our knowledge, the best resolution achieved for a high-speed OCT system in this wavelength band. We have shown the applications of our system in ophthalmology and cardiology, and have proposed other potential uses. We plan to investigate imaging and mapping the cardiac conduction system further, since we believe deep-penetration UHR-OCT is a promising tool to intraoperatively assist cardiac surgeons in discriminating specialized conduction tissue from surrounding muscle tissue. It is our hope that this can eliminate surgical heart block and the need for postoperative permanent pacing in children undergoing repair of congenital heart disease.

Bibliography

[1] D. Huang *et al.*, "Optical Coherence Tomography," *Science*, vol. 254, no. 5035, pp. 1178–1181, Nov. 1991.

[2] M. Adhi and J. S. Duker, "Optical coherence tomography – current and future applications," *Curr. Opin. Ophthalmol.*, vol. 24, no. 3, pp. 213–221, May 2013.

[3] F. Prati *et al.*, "Expert review document on methodology, terminology, and clinical applications of optical coherence tomography: physical principles, methodology of image acquisition, and clinical application for assessment of coronary arteries and atherosclerosis," *Eur. Heart J.*, vol. 31, no. 4, pp. 401–415, Feb. 2010.

[4] B. J. Vakoc, D. Fukumura, R. K. Jain, and B. E. Bouma, "Cancer imaging by optical coherence tomography: preclinical progress and clinical potential," *Nat. Rev. Cancer*, vol. 12, no. 5, pp. 363–368, May 2012.

[5] T. S. Kirtane and M. S. Wagh, "Endoscopic Optical Coherence Tomography (OCT): Advances in Gastrointestinal Imaging," *Gastroenterol. Res. Pract.*, vol. 2014, pp. 1–7, 2014.

[6] P. Targowski, B. Rouba, M. Góra, L. Tymińska-Widmer, J. Marczak, and A. Kowalczyk, "Optical coherence tomography in art diagnostics and restoration," *Appl. Phys. A*, vol. 92, no. 1, pp. 1–9, Jul. 2008.

[7] D. Stifter, "Beyond biomedicine: a review of alternative applications and developments for optical coherence tomography," *Appl. Phys. B*, vol. 88, no. 3, pp. 337–357, Aug. 2007.

[8] G. Schulz *et al.*, "Multimodal imaging of human cerebellum - merging X-ray phase microtomography, magnetic resonance microscopy and histology," *Sci. Rep.*, vol. 2, p. 826, Nov. 2012.

[9] L. Liu *et al.*, "Imaging the subcellular structure of human coronary atherosclerosis using micro–optical coherence tomography," *Nat. Med.*, vol. 17, no. 8, pp. 1010–1014, Aug. 2011.

[10] P. J. Marchand *et al.*, "Visible spectrum extended-focus optical coherence microscopy for label-free sub-cellular tomography," *Biomed. Opt. Express*, vol. 8, no. 7, pp. 3343–3359, Jun. 2017.

[11] A. Federici and A. Dubois, "Full-field optical coherence microscopy with optimized ultrahigh spatial resolution," *Opt. Lett.*, vol. 40, no. 22, pp. 5347–5350, Nov. 2015.

[12] S. L. Jacques, "Optical properties of biological tissues: a review," *Phys. Med. Biol.*, vol. 58, no. 11, p. R37, 2013.

[13] J. M. Schmitt, A. Knuttel, M. Yadlowsky, and M. A. Eckhaus, "Optical-coherence tomography of a dense tissue: statistics of attenuation and backscattering," *Phys. Med. Biol.*, vol. 39, no. 10, p. 1705, 1994.

[14] Laser Institute of America, *American National Standard for Safe Use of Lasers*. Orlando, FL: Laser Institute of America, 2014.

[15] K. Bizheva *et al.*, "Compact, broad-bandwidth fiber laser for sub-2-μm axial resolution optical coherence tomography in the 1300-nm wavelength region," *Opt. Lett.*, vol. 28, no. 9, pp. 707–709, May 2003.

[16] K. Q. Kieu, N. N. Peyghambarian, J. Klein, J. K. Barton, and A. Evans, "Ultrahigh resolution all-reflective optical coherence tomography system with a compact fiber-based supercontinuum source," *J. Biomed. Opt.*, vol. 16, no. 10, p. 106004, Oct. 2011.

[17] Thorlabs, Inc., "OCT Selection Guide." [Online]. Available: https://www.thorlabs.com/newgrouppage9.cfm?objectgroup_id=5702. [Accessed: 29-Jan-2018].

[18] R. K. Wang and A. L. Nuttall, "Phase-sensitive optical coherence tomography imaging of the tissue motion within the organ of Corti at a subnanometer scale: a preliminary study," *J. Biomed. Opt.*, vol. 15, no. 5, 2010.

[19] H. Y. Lee, P. D. Raphael, J. Park, A. K. Ellerbee, B. E. Applegate, and J. S. Oghalai, "Noninvasive in vivo imaging reveals differences between tectorial membrane and basilar membrane traveling waves in the mouse cochlea," *Proc. Natl. Acad. Sci. U. S. A.*, vol. 112, no. 10, pp. 3128–3133, Mar. 2015.

[20] W. Drexler and J. G. Fujimoto, Eds., *Optical Coherence Tomography*. Cham: Springer International Publishing, 2015.

[21] J. F. de Boer, B. Cense, B. H. Park, M. C. Pierce, G. J. Tearney, and B. E. Bouma, "Improved signal-to-noise ratio in spectral-domain compared with time-domain optical coherence tomography," *Opt. Lett.*, vol. 28, no. 21, pp. 2067–2069, Nov. 2003.

[22] R. Leitgeb, C. K. Hitzenberger, and A. F. Fercher, "Performance of fourier domain vs. time domain optical coherence tomography," *Opt. Express*, vol. 11, no. 8, pp. 889–894, Apr. 2003.

[23] M. A. Choma, M. V. Sarunic, C. Yang, and J. A. Izatt, "Sensitivity advantage of swept source and Fourier domain optical coherence tomography," *Opt. Express*, vol. 11, no. 18, pp. 2183–2189, Sep. 2003.

[24] H. A. Haus, *Waves and Fields in Optoelectronics*. Englewood Cliffs, New Jersey: Prentice-Hall, 1984.

[25] B. E. A. Saleh and M. C. Teich, *Fundamentals of Photonics*, Second Edition. Hoboken, New Jersey: John Wiley & Sons, 2007.

[26] H. Kawagoe, M. Yamanaka, S. Makita, Y. Yasuno, and N. Nishizawa, "High-resolution and deep-tissue imaging with full-range, ultrahigh-resolution spectral-domain optical coherence tomography in 1.7 um wavelength region (Conference Presentation)," in *Optical Coherence Tomography and Coherence Domain Optical Methods in Biomedicine XXI*, 2017, vol. 10053, p. 100531V.

[27] M. Wojtkowski, A. Kowalczyk, R. Leitgeb, and A. F. Fercher, "Full range complex spectral optical coherence tomography technique in eye imaging," *Opt. Lett.*, vol. 27, no. 16, pp. 1415–1417, Aug. 2002.

[28] Y. Yasuno, S. Makita, T. Endo, G. Aoki, M. Itoh, and T. Yatagai, "Simultaneous B-M-mode scanning method for real-time full-range Fourier domain optical coherence tomography," *Appl. Opt.*, vol. 45, no. 8, pp. 1861–1865, Mar. 2006.

[29] S. H. Yun, G. J. Tearney, J. F. de Boer, N. Iftimia, and B. E. Bouma, "High-speed optical frequency-domain imaging," *Opt. Express*, vol. 11, no. 22, pp. 2953–2963, Nov. 2003.

[30] M. Maria *et al.*, "Ultra-low noise supercontinuum source for ultra-high resolution optical coherence tomography at 1300 nm," 2018, p. 22.

[31] "Conduction System of the Heart," *Medical Dictionary*. Farlex and Partners, 2009.

[32] L. S. Costanzo, *Physiology*, 6th ed. Philadelphia, PA: Elsevier, 2018.

[33] D. Sánchez-Quintana and S. Y. Ho, "Anatomy of Cardiac Nodes and Atrioventricular Specialized Conduction System," p. 8.

[34] L. Liberman, E. S. Silver, P. J. Chai, and B. R. Anderson, "Incidence and characteristics of heart block after heart surgery in pediatric patients: A multicenter study," *J. Thorac. Cardiovasc. Surg.*, vol. 152, no. 1, pp. 197–202, Jul. 2016.

[35] R. S. Mosca, "Cardiopulmonary bypass, cardioplegia, confocal inspection...?," *J. Thorac. Cardiovasc. Surg.*, vol. 152, no. 1, pp. 203–204, Jul. 2016.

[36] C. M. Ambrosi, V. V. Fedorov, R. B. Schuessler, A. M. Rollins, and I. R. Efimov, "Quantification of fiber orientation in the canine atrial pacemaker complex using optical coherence tomography," *J. Biomed. Opt.*, vol. 17, no. 7, Jul. 2012.

[37] X. Yao, Y. Gan, C. C. Marboe, and C. P. Hendon, "Myocardial imaging using ultrahigh-resolution spectral domain optical coherence tomography," *J. Biomed. Opt.*, vol. 21, no. 6, p. 061006, Mar. 2016.

[38] I. P. Herman, "Sound, Speech, and Hearing," in *Physics of the Human Body*, Springer, Cham, 2016, pp. 657–730.

[39] N. Gerber *et al.*, "A multiscale imaging and modelling dataset of the human inner ear," *Sci. Data*, vol. 4, p. 170132, Sep. 2017.

[40] D. S. Thylur, R. E. Jacobs, J. L. Go, A. W. Toga, and J. K. Niparko, "Ultra-High-Field Magnetic Resonance Imaging of the Human Inner Ear at 11.7 Tesla," *Otol. Neurotol. Off. Publ. Am. Otol. Soc. Am. Neurotol. Soc. Eur. Acad. Otol. Neurotol.*, vol. 38, no. 1, p. 133, Jan. 2017.

[41] L. Ng, M. W. Kelley, and D. Forrest, "Making sense with thyroid hormone—the role of T_3 in auditory development," *Nat. Rev. Endocrinol.*, vol. 9, no. 5, p. 296, May 2013.

[42] J. S. Iyer *et al.*, "Micro-optical coherence tomography of the mammalian cochlea," *Sci. Rep.*, vol. 6, no. 1, Dec. 2016.

[43] PubMed Health Glossary, "Eye - National Library of Medicine," *PubMed Health*. [Online]. Available: https://www.ncbi.nlm.nih.gov/pubmedhealth/PMHT0022375/. [Accessed: 28-Aug-2018].
[44] R. M. Werkmeister *et al.*, "Ultrahigh-resolution OCT imaging of the human cornea," *Biomed. Opt. Express*, vol. 8, no. 2, p. 1221, Feb. 2017.
[45] S. Radhakrishnan *et al.*, "Real-Time Optical Coherence Tomography of the Anterior Segment at 1310 nm," *Arch. Ophthalmol.*, vol. 119, no. 8, pp. 1179–1185, Aug. 2001.
[46] W. P. Nolan *et al.*, "Detection of Primary Angle Closure Using Anterior Segment Optical Coherence Tomography in Asian Eyes," *Ophthalmology*, vol. 114, no. 1, pp. 33–39, Jan. 2007.
[47] International Glaucoma Association, "Primary angle closure glaucoma," *Primary angle closure glaucoma*, 2017. [Online]. Available: https://www.glaucoma-association.com/about-glaucoma/types-of-glaucoma/acute-glaucoma. [Accessed: 28-Aug-2018].
[48] A. C. Day *et al.*, "The prevalence of primary angle closure glaucoma in European derived populations: a systematic review," *Br. J. Ophthalmol.*, vol. 96, no. 9, pp. 1162–1167, Sep. 2012.
[49] J.-W. Cheng, Y. Zong, Y.-Y. Zeng, and R.-L. Wei, "The Prevalence of Primary Angle Closure Glaucoma in Adult Asians: A Systematic Review and Meta-Analysis," *PLoS ONE*, vol. 9, no. 7, Jul. 2014.
[50] R. Sihota, N. C. Lakshmaiah, K. B. Walia, S. Sharma, J. Pailoor, and H. C. Agarwal, "The trabecular meshwork in acute and chronic angle closure glaucoma.," *Indian J. Ophthalmol.*, vol. 49, no. 4, p. 255, Dec. 2001.
[51] T. Hamanaka, K. Kasahara, and T. Takemura, "Histopathology of the trabecular meshwork and Schlemm's canal in primary angle-closure glaucoma," *Invest. Ophthalmol. Vis. Sci.*, vol. 52, no. 12, pp. 8849–8861, Nov. 2011.
[52] H.-T. Wong *et al.*, "High-Definition Optical Coherence Tomography Imaging of the Iridocorneal Angle of the Eye," *Arch. Ophthalmol.*, vol. 127, no. 3, pp. 256–260, Mar. 2009.
[53] E. W. Chang, J. B. Kobler, and S. H. Yun, "Subnanometer optical coherence tomographic vibrography," *Opt. Lett.*, vol. 37, no. 17, p. 3678, Sep. 2012.
[54] B. Cense *et al.*, "Ultrahigh-resolution high-speed retinal imaging using spectral-domain optical coherence tomography," *Opt. Express*, vol. 12, no. 11, p. 2435, May 2004.
[55] M. Wojtkowski, V. J. Srinivasan, T. H. Ko, J. G. Fujimoto, A. Kowalczyk, and J. S. Duker, "Ultrahigh-resolution, high-speed, Fourier domain optical coherence tomography and methods for dispersion compensation," *Opt. Express*, vol. 12, no. 11, pp. 2404–2422, May 2004.
[56] S. Makita, T. Fabritius, and Y. Yasuno, "Full-range, high-speed, high-resolution 1-μm spectral-domain optical coherence tomography using BM-scan

for volumetric imaging of the human posterior eye," *Opt. Express*, vol. 16, no. 12, pp. 8406–8420, Jun. 2008.
[57] F. J. Harris, "On the use of windows for harmonic analysis with the discrete Fourier transform," *Proc. IEEE*, vol. 66, no. 1, pp. 51–83, Jan. 1978.
[58] S. H. Yun, G. J. Tearney, B. E. Bouma, B. H. Park, and J. F. de Boer, "High-speed spectral-domain optical coherence tomography at 1.3 μm wavelength," *Opt. Express*, vol. 11, no. 26, pp. 3598–3604, Dec. 2003.
[59] S. J. Crick, M. N. Sheppard, S. Y. Ho, L. Gebstein, and R. H. Anderson, "Anatomy of the pig heart: comparisons with normal human cardiac structure," *J. Anat.*, vol. 193, no. 1, pp. 105–119, Jul. 1998.
[60] E. Bo *et al.*, "Depth-of-focus extension in optical coherence tomography via multiple aperture synthesis," *Optica*, vol. 4, no. 7, pp. 701–706, Jul. 2017.
[61] B. I. Akca *et al.*, "Observation of sound-induced corneal vibrational modes by optical coherence tomography," *Biomed. Opt. Express*, vol. 6, no. 9, pp. 3313–3319, Aug. 2015.